Dual midbrain and forebrain origins of thalamic inhibitory interneurons

Polona Jager[1], Gerald Moore[2], Padraic Calpin[3], Xhuljana Durmishi[1], Yoshiaki Kita[4], Irene Salgarella[1], Yan Wang[4], Simon R. Schultz[2], Stephen Brickley[2], Tomomi Shimogori[4], Alessio Delogu[1]*

[1] Department of Basic and Clinical Neuroscience, Institute of Psychiatry, Psychology and Neuroscience, King's College London, London, UK

[2] Department of Life Sciences and Centre for Neurotechnology, Imperial College London, London, SW7 2AZ, UK

[3] Department of Physics and Astronomy, University College London, London, UK

[4] RIKEN, Center for Brain Science (CBS), Saitama, Japan

* Correspondence: alessio.delogu@kcl.ac.uk

Abstract

The proportion and distribution of local inhibitory neurons (interneurons) in the thalamus varies widely across mammals. The ubiquitous presence of interneurons in the thalamus of primates contrasts with the extreme sparsity of interneurons reported in mice and other small-brained mammals. This is reflected in the structure and function of thalamic local circuits, which are more complex in primates compared to rodents. To what extent the broad range of interneuron densities observed in mammalian species reflect the appearance of novel interneuron types or the elaboration of a plesiomorphic ontogenetic program, remains unclear.

Here, we identify a larger than expected complexity and distribution of interneurons across the mouse thalamus, where all thalamic interneurons can be traced back to two developmental programs: one specified in the midbrain and the other in the forebrain. Interneurons migrate to functionally distinct thalamocortical nuclei depending on their origin the abundant, midbrain-derived class populates the first and higher order sensory thalamus while the rarer, forebrain-generated class is restricted to some higher order associative regions. We also observe that markers for the midbrain-born class are abundantly expressed throughout the thalamus of the New World monkey marmoset. These data therefore reveal that, despite the broad variability in interneuron density across mammalian species, the blueprint of the ontogenetic organization of thalamic interneurons of larger-brained mammals exists and can be studied in mice.

Introduction

The thalamus is a forebrain structure that develops from the diencephalic prosomere 2 (p2) (Puelles and Rubenstein, 2003; Shi et al., 2017; Wong et al., 2018) and is primarily composed of cortically projecting excitatory thalamocortical (TC) neurons, divided into more than 30

individual nuclei in mammals (Clascá et al., 2012; Hunnicutt et al., 2014; Jones, 2007). The function of the thalamus has been historically described as relay of sensory information to the cortex (Cheong et al., 2013; Hubel and Wiesel, 1962; Piscopo et al., 2013; Shatz, 1996; Sherman and Guillery, 2002; Van der Loos and Woolsey, 1973; Zeater et al., 2015). Taking into account the diversity of input and output features of thalamocortical circuits (Clascá et al., 2012; Guillery, 1995; Herkenham, 1980; Rubio-Garrido et al., 2009; Sherman, 2016), more recent work has shown that the thalamus is also critically involved in cognitive processes allowing for behavioural flexibility (Bolkan et al., 2017; Groh et al., 2014; Guo et al., 2017; Ling et al., 2015; Rikhye et al., 2018a; Rikhye et al., 2018b; Saalmann and Kastner, 2011; Schmitt et al., 2017; Sherman, 2016).

In contrast to cortical networks, excitatory neurons in the thalamus do not connect with each other (Bickford et al., 2008; Hirsch et al., 2015; Jones, 2007; Rikhye et al., 2018b). Instead, local connections and computations within thalamocortical circuits are dominated by the resident inhibitory, GABA-releasing neurons (interneurons) (Hirsch et al., 2015; Montero, 1987; Pasik et al., 1976; Sherman, 2004).

Interneuron numbers and distribution vary widely across species, suggesting that they are critically involved in the evolution of thalamocortical structure and function (Arcelli et al., 1997; Letinic and Rakic, 2001; Rikhye et al., 2018b). In particular, comparative studies across all amniotes (reptiles, birds and mammals) have described a correlation between the proportion of interneurons and the size and connectivity of the excitatory thalamus (Arcelli et al., 1997; Butler, 2008).

For example, in the reptilian thalamus, which is mostly devoid of descending projections from the cortex, interneurons have only been identified in the retinorecipient regions (Butler, 2008; Kenigfest et al., 1995; Kenigfest et al., 1998; Pritz and Stritzel, 1994; Rio et al., 1992). In birds however, where reciprocal connections between the thalamus and the cortex are more abundant, thalamic interneurons are distributed more widely (Butler, 2008; Granda and Crossland, 1989; Veenman and Reiner, 1994).

Similarly among mammals, interneurons are largely restricted to the visual thalamus in smaller-brained marsupials, bats and mice, where they represent only 6% of the total neuronal population (Butler, 2008; Evangelio et al., 2018; Seabrook et al., 2013b). In primates, on the other hand, where higher order (HO) nuclei driven by cortical inputs are expanded relative to sensory relay (first order, FO) regions (Armstrong, 1979; Baldwin et al., 2017; Butler, 2008; Halley and Krubitzer, 2019; Stephan et al., 1981), interneurons are present across the entire thalamus and their proportion increases to around 30% (Arcelli et al., 1997; Braak and Bachmann, 1985).

To what extent these differences are the result of species-specific ontogenesis of thalamic interneurons remains poorly understood. We have previously shown that in the mouse, interneurons in the FO visual thalamus, the dorsal lateral geniculate nucleus (LGd), originate in the midbrain from an *En1*$^+$*Gata2*$^+$*Otx2*$^+$*Sox14*$^+$ lineage (Jager et al., 2016). On the other hand, earlier work in humans has suggested the DLX1/2-expressing ganglionic eminences (GE) in the telencephalon as the source of interneurons for some of the larger HO thalamic nuclei - the mediodorsal nucleus (MD) and the pulvinar (Letinić and Kostović, 1997; Letinic and Rakic, 2001; Rakić and Sidman, 1969). At the same time, the latter studies were not able to detect any such migration from the GE in the mouse and macaque brain (Letinic and Rakic, 2001). While these findings therefore point to innovation in developmental origins, we currently lack an understanding of the shared ontogeny of mammalian thalamic interneurons.

Here we hypothesized that a blueprint of the complex organization of thalamic interneurons observed in large-brained mammals is present even in the simpler thalamus of the mouse. This prediction is supported by findings from the cortex demonstrating that its inhibitory interneuron classes, generated in the subpallium and defined through expression of regulatory programs (i.e. transcription factors), are common to the amniote lineages (Arendt et al., 2019; Métin et al., 2007; Tasic et al., 2018; Tosches et al., 2018). Moreover, a conserved subpallial origin was demonstrated for cortical interneurons in the cyclostome hagfish, and therefore appears to be an ancestral feature of the vertebrate brain (Sugahara et al., 2017; Sugahara et al., 2016).

Using genetic fate mapping, 2-photon whole brain tomography and spatial modeling, we investigated the ontogeny and distribution of thalamic GABAergic interneurons comprehensively across the mouse thalamocortical nuclei. We then used fluorescent *in situ* marker detection to compare the distribution of genetically defined interneuron classes in the New World marmoset monkey brain. These experiments identify in the mouse a wider distribution of GABAergic interneurons than previously reported (Arcelli et al., 1997; Evangelio et al., 2018; Seabrook et al., 2013b), encompassing both FO sensory relay and HO thalamic nuclei, including associative HO nuclei that are most enlarged in primates. We then show that while the largest proportion of thalamic interneurons in the mouse is generated in the *En1*$^+$*Sox14*$^+$ embryonic midbrain, there is an additional class that derives from the *Nkx2.1*$^-$ *Dlx5*$^+$ inhibitory progenitor domains in the forebrain. Intriguingly, we also find that in the mouse interneurons are organized in a spatial pattern according to their ontogeny, such that midbrain-born interneurons are largely found in the principal sensory relays and modality related HO nuclei, while the forebrain-generated interneurons reside in the HO thalamus, including MD, laterodorsal (LD) and lateral posterior (LP; aka pulvinar). Genoarchitectonic evidence supports

a conserved basic organization of thalamic interneurons in the non-human primate marmoset thalamus, where putative midbrain-generated interneurons are abundant in FO and HO nuclei and complemented by a distinct and more restricted interneuron class enriched in selected HO associative TC nuclei.

Results

Sox14-expressing interneurons are widely distributed across the first and higher order mouse thalamus.

In the mouse thalamus, GABAergic interneurons are most abundant in the LGd (Arcelli et al., 1997; Evangelio et al., 2018). We had previously demonstrated that all LGd interneurons are defined by expression of the transcription factor gene *Sox14* and presented the *Sox14*$^{GFP/+}$ knockin mouse line (Crone et al., 2008) as a useful tool to study these cells (Jager et al., 2016). Both the Allen Brain Atlas (© 2015 Allen Institute for Brain Science. Allen Cell Types Database. Available from: celltypes.brain-map.org) and DropViz resources [available from: dropviz.org; (Saunders et al., 2018)] identify a *Sox14*$^{+}$ transcriptional cluster corresponding to mouse LGd interneurons, confirming our previous findings. *Sox14* is expressed upon cell-cycle exit within inhibitory lineages in the diencephalon, midbrain, hindbrain and spinal cord, but not in the telencephalon (Achim et al., 2013; Delogu et al., 2012; Guo and Li, 2019; Prekop et al., 2018).

To investigate the spatial distribution of *Sox14* neurons comprehensively across all thalamic (thalamocortical, TC) regions in the mouse, we took advantage of the endogenous and bright fluorescence of GFP in postnatal day (P) 21 *Sox14*$^{GFP/+}$ mice to perform high resolution (0.54 μm voxel) whole brain imaging by 2-photon laser scanning tomography; for an indicative low resolution scan through a series of z-projections see: Supp. Movie 1. Optical sections were acquired in the coronal plane 10μm apart and registered with the Allen Institute Common Coordinate Framework (CCF3) using a custom Python pipeline alongside the Elastix registration library (Klein et al., 2010) to delineate anatomical subdivisions according to the Allen Brain Institute taxonomy (Supp. Movie 2). To perform automated detection of cells, a deep learning strategy was implemented to train a U-Net segmentation model (Ronneberger, Fischer, & Brox, 2015) on a dataset of 12264 images (512 × 512 pixels at 0.54 μm voxel), obtained by supplemental augmentation of 219 manually annotated samples. The accuracy of our automated counting strategy was validated by comparing the total count of GFP^{+} cells in the LGd of P21 *Sox14*$^{GFP/+}$ mice (1234 ± 82; mean ± SD) to a recent stereological study of LGd GABA interneurons in the wild type adult C57Bl/6 mouse (1255 ± 195; mean ± SD) (Evangelio et al., 2018), which confirmed the validity of our protocol.

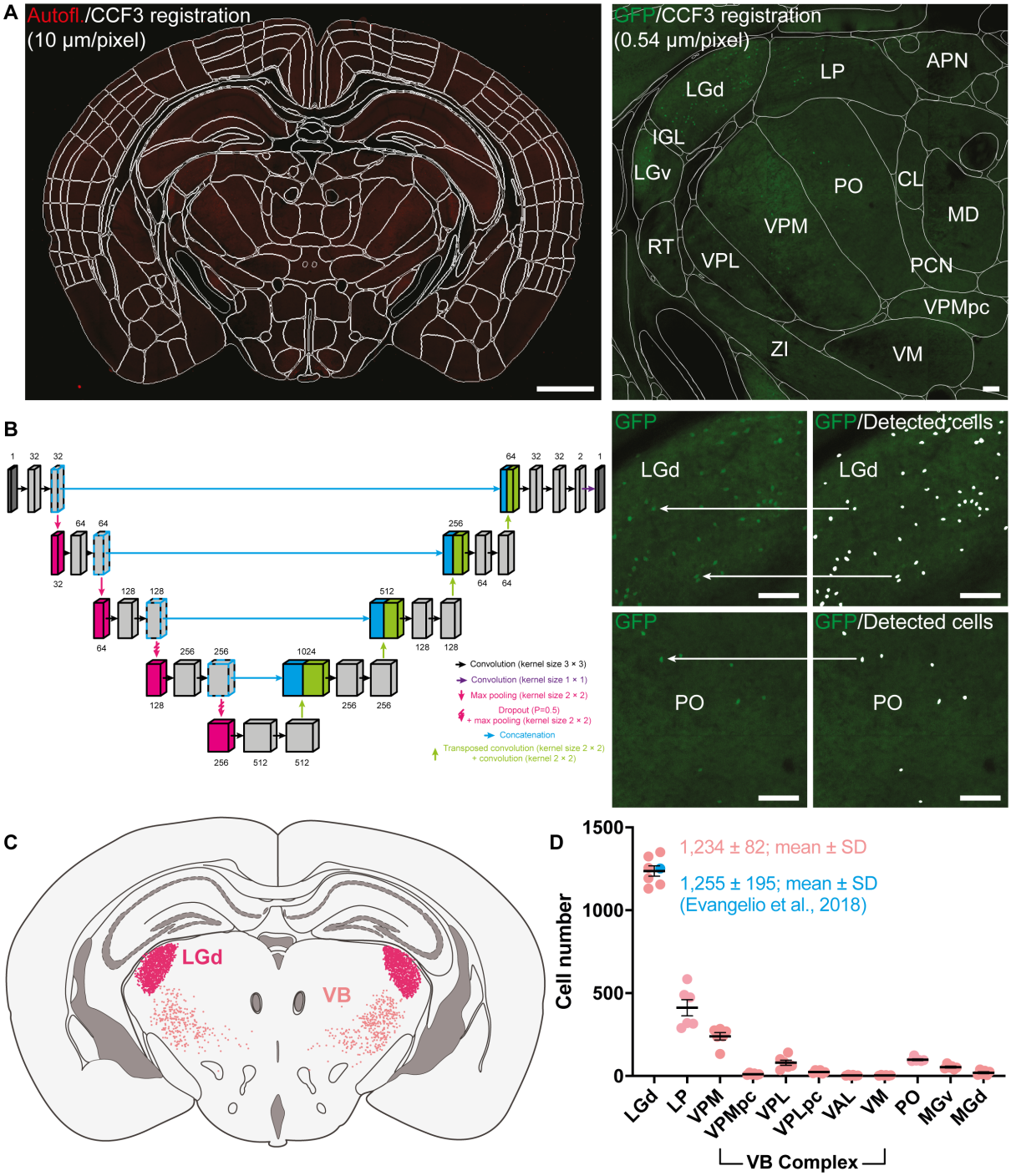

Figure 1. Automated total counts of GFP^{+} cells in the thalamus of the Sox14$^{GFP/+}$ mouse. **A**. Autofluorescence (Autofl.) from serial two-photon imaging of Sox14GFP/+ mice (n=3) at 0.54 × 0.54 × 10 µm voxel resolution was registered to the Allen Institute CCF3 atlas using Elastix (left; scale bar 1 mm). This permits delineation and identification of all anatomical structures according to the Allen Institute hierarchical taxonomy (right; scale bar 100 µm). **B**. Automated cell detection was done using a U-Net trained on 219 manually segmented images (512 × 512 pixels) augmented to a total sample size of 12,264, split 75% for training and 25% validation. Images containing GFP fluorescence were passed into the trained U-Net (left) for cell prediction based on learned features during training (right; scale bar 100 µm). Oversampling in the z-axis was corrected for by grouping and averaging detected cell positions which colocalised within a defined cell radius. **C**. Example illustration of automatically detected cells in the LGd and VB complex projected onto a representative coronal section of

the thalamus. **D**. Quantification of GFP$^+$ cells in the LGd at 1234 ± 82 (mean ± SD) validated against stereological study by Evangelio et al. (2018) of 1255 ± 195 (mean ± SD) interneurons in the LGd. Other counts are shown for LP, VB complex [VPM, parvicellular part of the ventral posteromedial nucleus (VPMpc), VPL, parvicellular part of the ventral posterolateral nucleus (VPLpc), VAL, VM], MGv, MGd, and PO.

Automated counting identified a total of 6588 ± 811 (mean ± SEM) GFP$^+$ cells across TC nuclei of both hemispheres spanning the rostrocaudal and mediolateral extensions of the thalamus (n=3 *Sox14*$^{GFP/+}$ at P21). Their distribution was not stochastic but skewed instead towards sensory TC nuclei and, within sensory modality, by a prevalence in FO nuclei. The GFP$^+$ cells are most abundant in the visual FO LGd (1234 ± 82) and HO lateral posterior (LP aka pulvinar; 411 ± 110), followed by sensory-motor ventrobasal complex (VB) [ventral posteromedial (VPM; 250 ± 49), ventral posterolateral (VPL; 105 ± 40) ventral anterior lateral (VAL; 4 ± 3) and ventral medial (VM; 4 ± 2)] and HO posterior (PO; 99 ± 12) in turn followed by the auditory FO ventral medial geniculate (MGv; 53 ± 12) and HO dorsal medial geniculate (MGd; 20 ± 13). Sparse GFP$^+$ cells were also detected in limbic TC nuclei: laterodorsal (LD; 20 ± 7), parafascicular (PF; 25 ± 5) and mediodorsal (MD; 13 ± 6). Notably, GFP$^+$ neurons are typically found in the caudal-most part of the LD, nearer the LP border and nearly all GFP$^+$ neurons were in the caudal half of the MD (see also Supp. Movie 1). Counts are reported for a single hemisphere.

***Sox14* expression distinguishes between two spatially clustered interneuron classes**

To validate the inhibitory nature of the GFP$^+$ cells in TC nuclei of the *Sox14*$^{GFP/+}$ mouse, we combined immunodetection of GFP$^+$ with in situ RNA hybridization against the *Gad1* mRNA in *Sox14*$^{GFP/+}$ mice sampling the rostrocaudal extent of the thalamus at aproximately 200 μm intervals (Fig. 2A-C). In our experience, the simultaneous detection of protein and mRNA is more reliable in younger tissue, hence experiments were done at P14, by which timepoint mouse TC nuclei are considered to display adult-like circuit composition (Bickford et al., 2010; Golding et al., 2014; Seabrook et al., 2013a; Seabrook et al., 2013b; Thompson et al., 2016). Recapitulating the distribution observed at P21, GFP$^+$ cells were detected in the LGd, LP, VP, PO and in very small numbers in the MG (Fig. 2A,C,D). In these nuclei all GFP$^+$ cells had a GABAergic profile and co-expressed *Gad1* (100%, n=3 brains). In the LGd, VP and MGv (i.e. FO sensory relay nuclei) they also represented virtually all GABAergic cells (≥98%, pie charts in Fig. 2D).

Unexpectedly however, 22.1±4.0% of the total GABAergic population in TC regions did not express GFP (Fig. 2B,C; 3Bii), and these GFP$^-$*Gad1*$^+$ cells appeared spatially largely non-overlapping with the *Sox14*$^+$ interneuron class (Fig. 2C,D). In particular, we observed that the distribution of GFP$^-$*Gad1*$^+$ cells is skewed towards the limbic HO MD (29.6±4.5%) and LD

(19.4±3.1%) and the associative HO LP (13.2±1.2%), and in smaller numbers in the PO. Sparse GFP$^-$Gad1$^+$ cells were also found in thalamic regions where nuclear boundaries cannot be defined precisely at this age and that contain: VAL, VM, centrolateral (CL), intermediodorsal (IMD), parafascicular (PF), reuniens (RE), romboid (RH), subparafascicular (SPF), subparafascicular area (SPA), central medial (CM), anteromedial (AM), cell counts in these regions were grouped together under "other TC" (Fig. 2D).

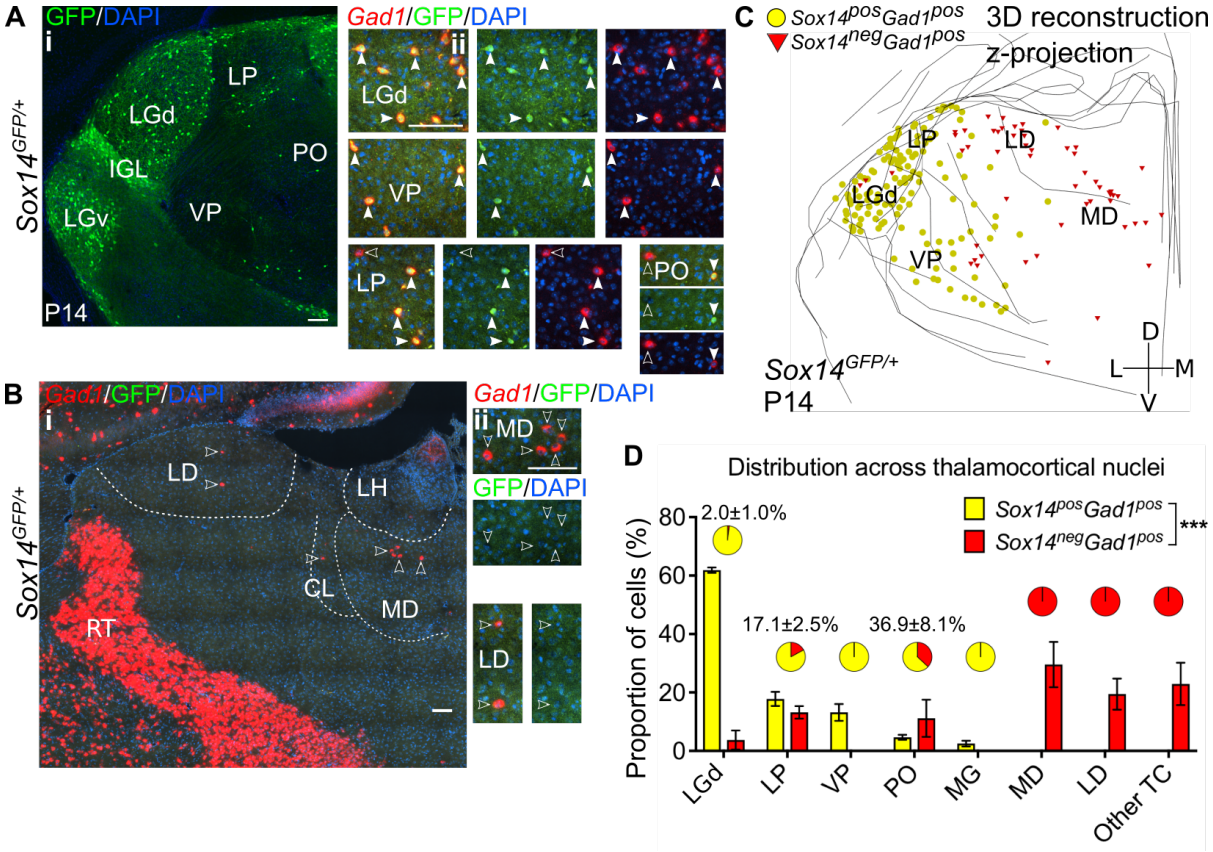

Figure 2. Diversity and distribution of GABAergic cells in the mouse thalamocortical nuclei. A. (i) Representative coronal section of P14 *Sox14*$^{GFP/+}$ thalamus with *Sox14*$^+$ cells in the LGd, VP, LP and PO. (ii) *Sox14*$^+$ cells in TC regions co-express *Gad1*, but not all *Gad1*$^+$ cells co-express *Sox14* in the LP and PO. Filled arrows mark *Sox14*$^+$*Gad1*$^+$ and empty arrows *Sox14*$^-$*Gad1*$^+$ cells. Scale bars, 100 µm. **B.** (i) Representative rostral coronal section of P14 *Sox14*$^{GFP/+}$ thalamus with *Gad1*$^+$ cells in the MD, CL and LD, and containing no *Sox14*$^+$ cells. (ii) *Gad1*$^+$ cells in these nuclei do not co-express *Sox14*. Scale bars, 100 µm. **C.** 3D reconstruction of a representative P14 *Sox14*$^{GFP/+}$ thalamus from tracing every tenth 20µm-thick coronal section, displayed as a z-projection and showing distribution of *Sox14*$^+$*Gad1*$^+$ (yellow) and *Sox14*$^-$*Gad1*$^+$ cells (red). One dot represents one neuron. **D.** Distribution of *Sox14*$^+$*Gad1*$^+$ and *Sox14*$^-$*Gad1*$^+$ cells across TC nuclei in the *Sox14*$^{GFP/+}$ brains at P14, plotted as proportion of all the cells within each interneuron group (mean±SEM; n= 3 brains). The category "other TC" refers to regions where nuclear boundaries cannot be defined precisely and that contain VAL, VM, CL, IMD, PF, RE, RH, SPF, SPA, CM, AM. *Sox14*$^+$*Gad1*$^+$ and *Sox14*$^-$*Gad1*$^+$ populations have distinct distributions (p~0, Chi-squared test). Pie charts show the proportion (mean±SEM) of the two interneuron classes within each nucleus.

To quantitatively demonstrate spatial clustering of these two putative thalamic interneuron classes (*Gad1*$^+$*Sox14*$^+$ and *Gad1*$^+$*Sox14*$^-$), we calculated the nearest neighbour distances

(NND) from 3D reconstructions of their respective distributions in the *Sox14*$^{GFP/+}$ thalamus (Fig. 2A,C). Indeed, the cumulative distribution of NNDs was significantly shifted to smaller distances within each of the classes than between them ($p<1.4\times10^{-30}$, 2-sample Kolmogorov-Smirnov test, n=3 brains; Fig. 3A).

To characterise spatial organization of thalamic GABAergic interneurons in an unbiased way, we then applied machine learning (k-Means clustering) to these same 3D reconstructions of the *Sox14*$^{GFP/+}$ thalami (Fig. 2C). The data best fit two spatial clusters, as assessed from the silhouette score (Fig. 3Bii,C; see also Materials and Methods). Consistent with the NND analysis, one cluster corresponded to the *Sox14*$^{+}$ cells (contains 94.9±1.4% of all *Sox14*$^{+}$ cells), and the other to the *Sox14*$^{-}$ interneurons (contains 81.0±0.3% of all *Sox14*$^{-}$ cells; Fig. 3B,D). The two thalamic molecular GABAergic groups therefore occupy their own respective spatial clusters, with the *Sox14*$^{-}$ cells located more rostrally and medially compared to the *Sox14*$^{+}$ interneurons.

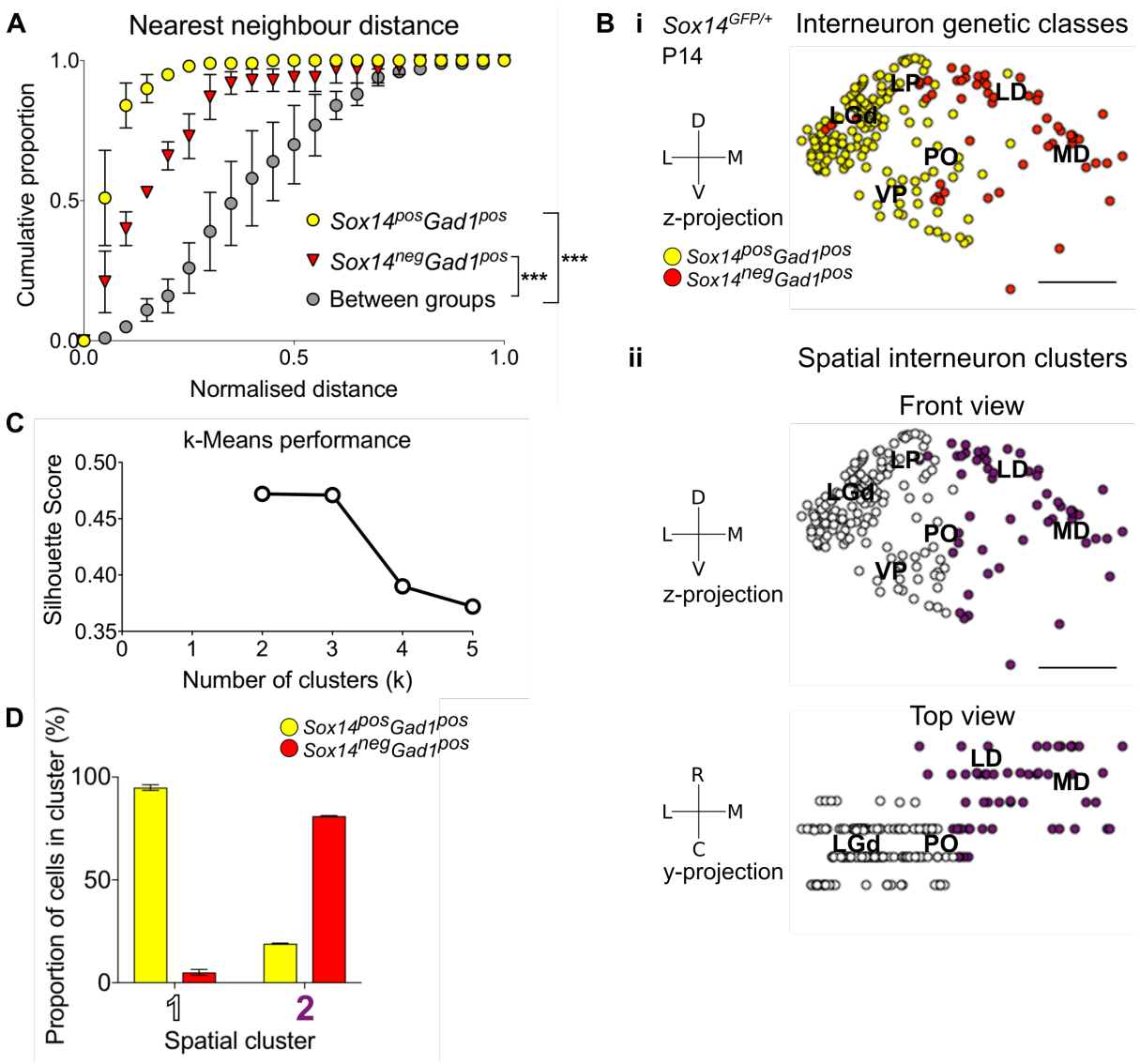

Figure 3. Spatial organization of thalamic GABAergic cells. A. Normalised nearest neighbour distance (NND) for *Sox14*$^{+}$*Gad1*$^{+}$ and *Sox14*$^{-}$*Gad1*$^{+}$ populations and between the two groups from P14 *Sox14*$^{GFP/+}$ data (Fig. 2), plotted as cumulative proportion of all cells within a given set. The NND distribution is significantly shifted to larger distances between groups than within each of the groups ($p<1.4\times10^{-30}$, 2-sample Kolmogorov-Smirnov test, n=3 brains). **B.** Representative z-projections of IN distribution amongst TC nuclei, from P14 *Sox14*$^{GFP/+}$ data (Fig. 2). One dot represents one neuron and they are colour-coded by (i) their genetic identity or (ii) spatial cluster. For the spatial clusters a y-projection is also shown. Scale bars, 500µm. **C.** Performance of unsupervised k-Means algorithm in identifying thalamic interneuron spatial clusters from the P14 *Sox14*$^{GFP/+}$ data (n=3 brains, see also Fig. 2) as measured by the silhouette score, which varies with number of clusters (k). We choose k=2 as this point has the highest score. **D.** Proportion of *Sox14*$^{+}$ and *Sox14*$^{-}$ GABAergic cells in each spatial cluster, averaged over three brains (mean±SEM).

To independently confirm our findings and control for potential effects of looking at a juvenile age (P14), we also mapped anatomical distribution of all *Gad1*$^{+}$ and *Chrna6*$^{+}$ cells across the adult mouse TC nuclei at P56, using the Allen Mouse Brain Atlas (© 2004 Allen Institute for Brain Science. Allen Mouse Brain Atlas. Available from: mouse.brain-map.org; (Lein et al., 2006)) *in situ* hybridization data (Supp. Fig. 2). *Chrna6* has been identified as another marker specific for interneurons, at least in the LGd ((Golding et al., 2014); DropViz; Allen Cell Types Database). The resulting 3D reconstructions, k-Means spatial clustering (Supp. Fig. 2A) and distribution plot (Supp. Fig. 2B) were consistent with our observations from the P14 *Sox14*$^{GFP/+}$ thalamus.

The mouse thalamus therefore exhibits wider interneuron diversity than has been previously reported, with at least two molecularly and spatially distinct classes. The largest interneuron class is the defined by *Sox14*$^{+}$ and is enriched in the caudal half of the thalamus which contains principal sensory relays and their associated HO nuclei. Conversely, the smaller *Sox14*$^{-}$ GABAergic population is enriched in the rostral half of the thalamus, in HO regions that associate with more cognitive functions, such as the MD and LD (Halassa and Kastner, 2017; Rikhye et al., 2018a).

The *Sox14*$^{+}$ interneuron class is abundant and widespread in the marmoset brain

Given the sparseness of interneurons in the mouse thalamus, there exists the possibility that the *Sox14*$^{+}$ interneuron class may represent a unique feature of smaller-brained species, or that it may be a conserved, but numerically negligible type of interneuron complemented by novel and more abundant types in species with larger brains. To detect the presence and assess the relative abundance of the *Sox14*$^{+}$ interneuron class in the thalamus of species with a high density of interneurons, we sampled the distribution of *SOX14*$^{+}$*GAD1*$^{+}$ cells in selected TC nuclei of the neonatal non-human primate marmoset.

Fluorescent in situ hybridisation for *SOX14* and *GAD1* mRNAs revealed the widespread presence of *SOX14*$^+$*GAD1*$^+$ bona fide interneurons across all major TC nuclei (Fig. 4A,B,C). Reminiscent of the expression pattern observed in the mouse, *SOX14*$^+$ cells were not present in prethalamic structures [RT, zona incerta (ZI)], but detectable in the pregeniculate/subgeniculate (SubG), the primate homologue of the mouse IGL (Fig. 4B).

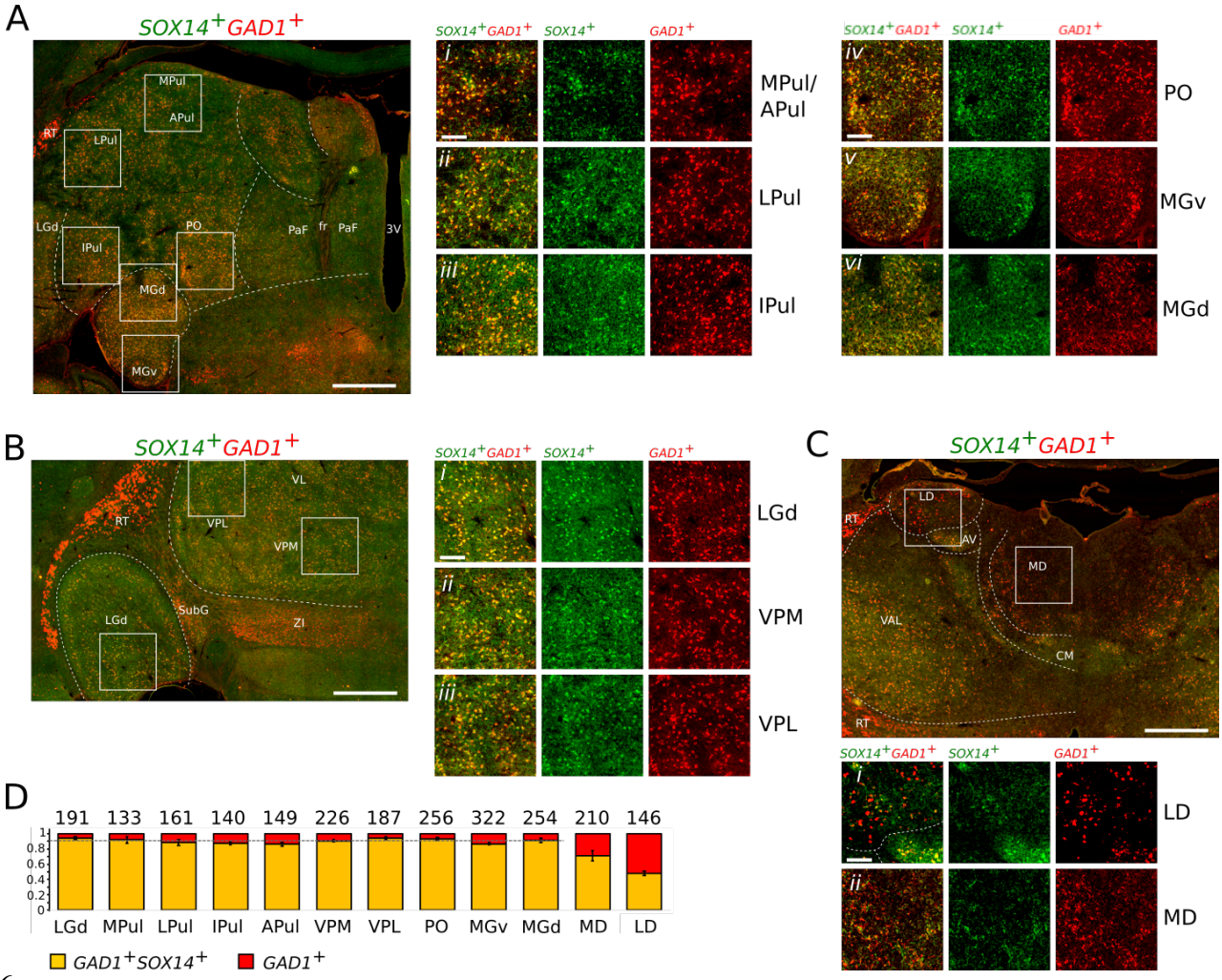

Figure 4. *SOX14*$^+$*GAD1*$^+$ interneurons dominate TC regions of the non-human primate marmoset. Representative coronal sections of the thalamus of a new-born marmoset illustrating the distribution of cells expressing the *SOX14* (green) and *GAD1* (red) mRNAs. **A.** Caudal plane containing subdivisions of the pulvinar complex, the PO and the auditory MG. Also visible are parafascicular (PaF) nuclei. Fr, fasciculus retroflexus; 3V, third ventricle. **A*i-iii***. Magnifications of indicative areas of the medial (MPul) and anterior pulvinar (APul), the lateral pulvinar (LPul) and inferior pulvinar (IPul). **A*iv***. Magnification of a region of the PO. **A*v-vi***. Magnifications of representative regions of the ventral (MGv) and dorsal (MGd) subdivisions of the auditory thalamus. **B**. Middle plane section containing the sensory TC nuclei LGd, VPM, VPL and other non-TC structures (ZI, RT and SubG). **B*i-iii*.** Magnifications illustrating the dominant presence of *SOX14*$^+$*GAD1*$^+$ interneurons in the sensory FO nuclei. **C.** Anterior plane containing the VAL, centromedial (CM), anteroventral (AV), LD and MD. The prethalamic RT is recognisable as an entirely *SOX14*$^-$*GAD1*$^+$ structure. **C*i***. Magnification of an area of the LD containing comparable densities of *SOX14*$^+$ and *SOX14*$^-$ interneurons. **C*ii***. Magnification of an area of the MD containing *SOX14*$^+$ and *SOX14*$^-$ interneurons. **D**. Fraction

of *SOX14*$^{+}$*GAD1*$^{+}$ (yellow) and *SOX14*$^{-}$*GAD1*$^{+}$ (red) interneurons in selected TC nuclei. Above each bar the total cell counts from 9 regions of interest (ROI) measuring 263μm by 263μm per each TC nucleus in 3 age-matched brains (3 ROI per TC nucleus/brain). The average fraction of *SOX14*$^{-}$*GAD1*$^{+}$ interneurons deviates significantly from background level in the MD and LD. Scale bars: low magnification overviews: ~1mm; magnified areas: ~0.2mm.

Qualitative analysis shows largely overlapping distribution of the fluorescent probes for *SOX14* and *GAD1* in all TC nuclei at caudal (Fig. 4A*i-vi*) and intermediated level (Fig. 4B*i-iii*), but some areas of differential expression at rostral level, where *GAD1* expression is not accompanied by *SOX14* expression in medial and dorsal regions of the thalamus (Fig. 4C) that contain the limbic HO TC nuclei LD (Fig. 4C*i*) and MD (Fig. 4C*ii*). We then proceeded to quantify the number of *SOX14*$^{+}$*GAD1*$^{+}$ and *SOX14*$^{-}$*GAD1*$^{+}$ cells in 3 brains of the new-born marmoset by randomly selecting 3 regions of (263μm by 263μm) within each FO visual LGd, HO visual and multimodal associative medial, lateral, inferior and anterior pulvinar subdivisions (MPul, LPul, IPul and APul, respectively), FO somatosensory VPM and VPL, HO sensory PO and auditory FO (MGv) and HO (MGd) as well as non-specific HO MD and LD. With the exception of the MD and LD, all TC nuclei tested contained mostly *SOX14*$^{+}$*GAD1*$^{+}$ cells (90.2%±0.9%; mean±SEM; dotted line in Fig 4D). This may in fact be an underestimate, due to the observed lower efficiency of the *SOX14* probe compared to the *GAD1*. Analysis of the frequency distribution of the two cell classes across the tested nuclei, reveals the MD and LD as outliers of an otherwise normal distribution (Motulsky and Brown, 2006). Indeed, in the MD and LD *SOX14*$^{-}$*GAD1*$^{+}$ cells account for 28.7%±6.7% and 52.3%±2.8% (mean±SEM) of the total GAD1^{+}, respectively (Fig. 4D). The presence of a sizeable population of *SOX14*$^{-}$*GAD1*$^{+}$ cells in the MD and LD is intriguing for their reminiscence of the forebrain-derived *Sox14*$^{-}$*Gad1*$^{+}$ interneurons of the mouse (Fig. 2C,D) which are also most abundant in these two non-specific HO nuclei.

We find the presence in both the mouse and marmoset of an abundant *SOX14*$^{+}$*GAD1*$^{+}$ interneuron class and the relative distribution of *SOX14*$^{+}$*GAD1*$^{+}$ and *GAD1*$^{+}$ single positive interneurons compatible with a conserved basic organisation of interneuron diversity in rodents and primates alike.

All *Sox14*-expressing thalamic interneurons are born in the midbrain

Given the known role of *Sox14* in specifying subcortical inhibitory classes (Achim et al., 2013; Delogu et al., 2012; Guo and Li, 2019; Prekop et al., 2018; Sellers et al., 2014) and following our identification of *Sox14* as a conserved genetic marker for the larger cohort of thalamic interneurons in both the primate and rodent brain, we investigated the requirement for this gene in interneurons across TC modalities and hierarchy in the *Sox14*$^{GFP/GFP}$ (*Sox14* knockout, KO) mouse. We have previously shown that in the Sox14 KO there is a >90% reduction in the

number of interneurons in the LGd (Jager et al., 2016). We find a comparable reduction in the number of *Sox14*$^{+}$ interneurons overall across the LGd, LP, VP, PO and MG in the *Sox14* KO (90.5±1.5%, p=2.7×10^{-4}, two-sample two-tailed t-test, n=3 brains/genotype; Fig. 5A,B). Conversely, there was no significant change in the number of *Sox14*$^{-}$*Gad1*$^{+}$ cells (p=0.4, two-sample two-tailed t-test; Fig. 5A,B) and in their distribution across TC regions (Fig. 5A,C; p>0.05, Chi-squared test, n=3 brains/genotype). These results therefore indicate that the two TC interneuron populations may already be segregated during development and represent two distinct GABAergic lineages.

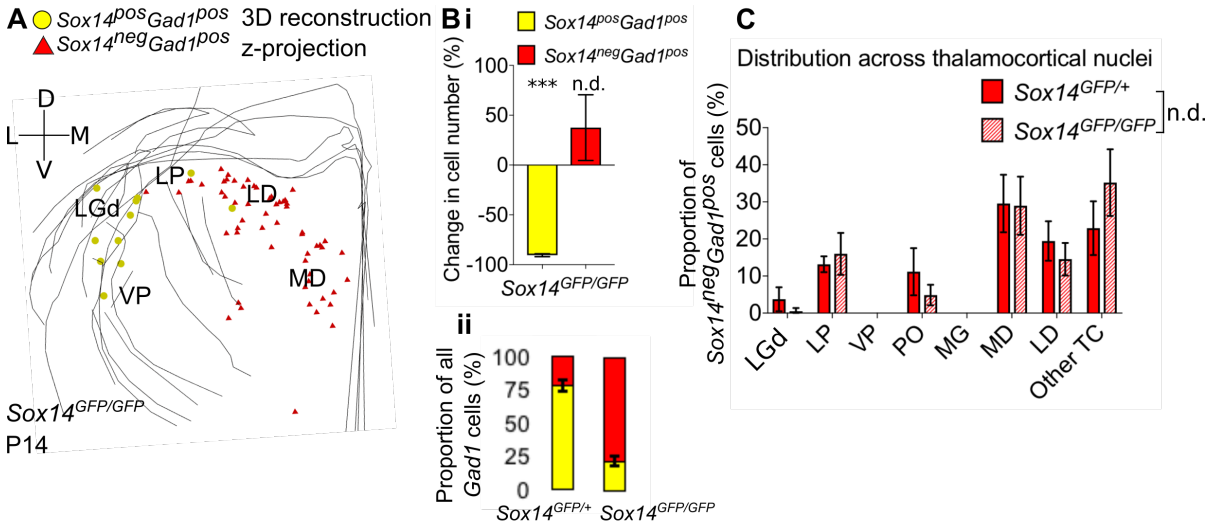

Figure 5. A. Differential requirement for Sox14 highlights two distinct developmental classes. 3D reconstruction of a representative P14 *Sox14*$^{GFP/GFP}$ thalamus from tracing every tenth 20µm-thick coronal section, displayed as a z-projection and showing distribution of *Sox14*$^{+}$*Gad1*$^{+}$ (yellow) and *Sox14*$^{-}$*Gad1*$^{+}$ cells (red). **B.** (i) Relative change in the number of *Sox14*$^{+}$*Gad1*$^{+}$ and *Sox14*$^{-}$*Gad1*$^{+}$ cells across TC regions in P14 *Sox14*$^{GFP/GFP}$ relative to P14 *Sox14*$^{GFP/+}$ data (mean±SEM, n=3 brains/genotype). There is a significant reduction in the *Sox14*$^{+}$*Gad1*$^{+}$ population (p=2.7×10^{-4}, two-sample two-tailed t-test), but no statistically significant difference in the size of the *Sox14*$^{-}$*Gad1*$^{+}$ group (p=0.4, two-sample two-tailed t-test). (ii) Proportion of *Sox14*$^{+}$*Gad1*$^{+}$ cells within the total GABAergic population is decreased in the *Sox14*$^{GFP/GFP}$ (mean±SEM, n=3 brains/genotype). **C.** Distribution of *Sox14*$^{-}$*Gad1*$^{+}$ cells across TC nuclei in the *Sox14*$^{GFP/+}$ and *Sox14*$^{GFP/GFP}$ brains at P14 (mean±SEM; n= 3 brains/genotype). *Sox14*$^{-}$*Gad1*$^{+}$ distribution is unaltered in the *Sox14* KO (p>0.05, Chi-squared test).

LGd interneurons in the mouse derive from the midbrain (Jager et al., 2016). To explore how the molecular and spatial organization of thalamic interneurons is generated during development more conclusively, we fate-mapped midbrain lineages and checked for their presence, distribution and inhibitory profile across the thalamus. We crossed *En1-Cre* (Kimmel et al., 2000) with a *R26lsl-GFP* (Sousa et al., 2009) reporter line (Fig. 6A), as the *En1* TF gene is expressed in the midbrain and rostral hindbrain progenitors, but not in the forebrain (Sgaier et al., 2007). Analysis of the thalamus at P21 reveals GFP^{+} cells (*En1*$^{+}$ lineage) distributed

across the LGd and co-expressing GABA (Fig. 6B), therefore independently validating our previous observation (Jager et al., 2016). However, like the *Sox14*$^{+}$*Gad1*$^{+}$ neurons, *En1*$^{+}$ cells were observed beyond the LGd - in the LP, VP, PO and MG, where they were also positive for GABA (Fig. 6B,C). Plotting their distribution confirmed that it is equivalent to the distribution of *Sox14*$^{+}$ INs (p>0.05, Chi-squared test; Fig. 6C,D). Occasional GFP^{+} cells with glia-like morphology were also observed in the thalamus. These cells were GABA^{-} and were not included in any of the analyses.

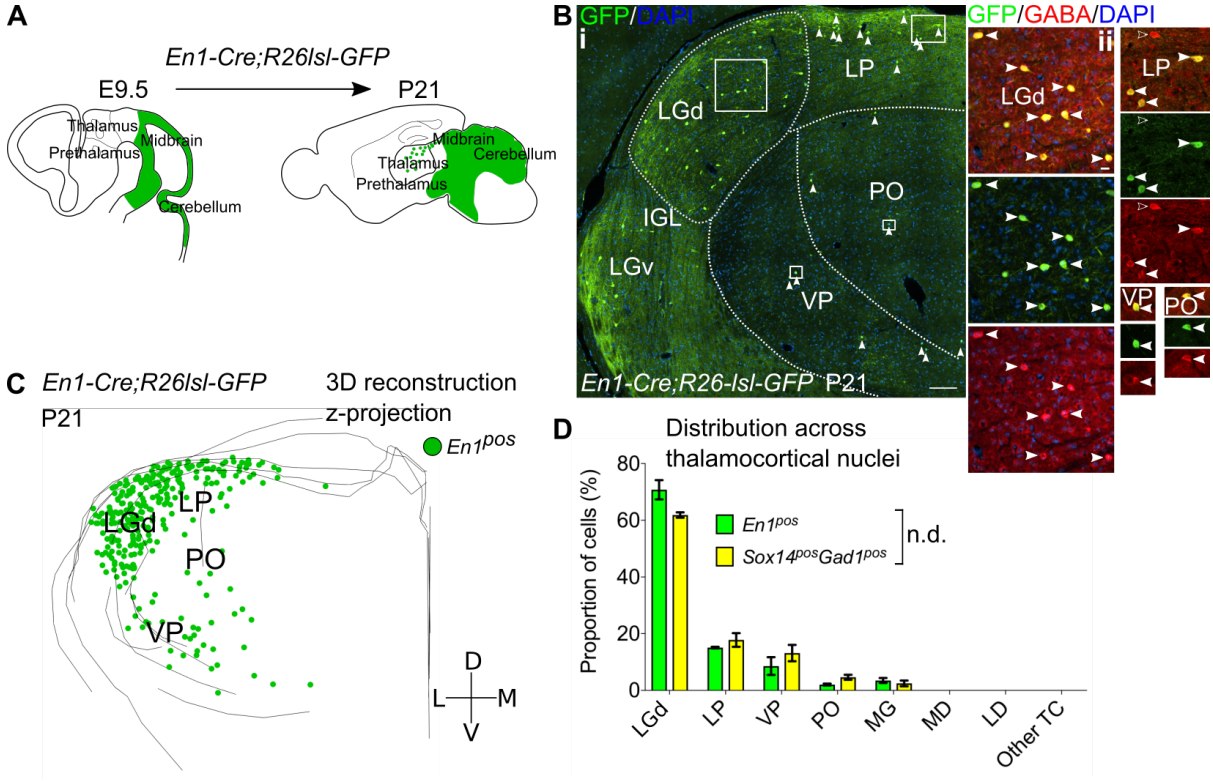

Figure 6. *Sox14*$^{+}$ interneurons in TC regions derive from the midbrain. **A.** Schematic of the fate mapping experiment: crossing *En1-Cre* with *R26lsl-GFP* reporter line permanently labels all midbrain born cells with GFP expression. **B.** (i) Representative coronal section of P21 *En1-Cre;R26lsl-GFP* thalamus with *En1*$^{+}$ cells observed in the LGd, LP, VP and PO (considering TC regions only). For clarity some of the *En1*$^{+}$ cells are indicated with white arrows. Scale bar, 100µm. (ii) *En1*$^{+}$ cells in these regions co-express GABA (filled white arrows). Empty arrows mark GABA single-positive cells. Scale bar, 10µm. **C.** 3D reconstruction of a representative P21 *En1-Cre;R26lsl-GFP* thalamus from tracing every sixth 60µm-thick coronal section, displayed as a z-projection and showing distribution of *En1*$^{+}$ cells. **D.** Distribution of *Sox14*$^{+}$*Gad1*$^{+}$ and *En1*$^{+}$ cells across TC nuclei in *Sox14*$^{GFP/+}$ and *En1-Cre;R26lsl-GFP* brains, respectively, plotted as proportion of all the cells within each group (mean±SEM; n= 3 brains/genotype). The two populations are not differently distributed (p>0.05, Chi-squared test).

We therefore conclude that the *Sox14*$^{+}$ thalamic interneurons across FO and HO TC nuclei all derive from the midbrain, and simultaneously that the *Sox14*$^{-}$ GABAergic cells do not; the two classes thus represent distinct inhibitory lineages in TC regions, further supporting their definition as two distinct thalamic interneuron classes.

Midbrain-derived interneurons migrate along two streams into the sensory thalamus during the first postnatal week

En1-Cre;R26lsl-GFP line was then used to investigate the timeline and spatial trajectories of the *Sox14*$^+$ interneuron precursors migrating from the midbrain into the first and higher order sensory TC regions (Fig. 7A). Previously, LGd interneurons were found to populate this nucleus in the first postnatal week (Golding et al., 2014; Jager et al., 2016). We therefore looked at the numbers and migratory morphology of GFP$^+$ (i.e. *En1*$^+$) cells in the thalamus at E16.5, E17.5, P0.5, P1.5 and P2.5. We focused on the LGd, LP and VP, but left out the PO and MG, due to low overall numbers of interneurons in these two regions (Fig. 2, Supp. Fig. 2).

At E16.5 no GFP$^+$ cells were present in the thalamus. From E17.5 to P2.5 their numbers progressively increased in all of the regions analysed (Fig. 7A,B). The number of GFP$^+$ cells in the LGd at P2.5 matched previous independent reports (Golding et al., 2014), validating our counting method. Midbrain-derived interneurons therefore populate the different TC regions following a similar timeline. Interestingly, they appear in two ventrally located nuclei (i.e. LGd and VP) simultaneously (Fig. 7A,B), implying they use distinct routes to reach them.

To infer their direction of migration, we determined the leading process orientation of migrating GFP$^+$ cells along all three dimensions (ventro-dorsal, latero-medial, caudo-rostral; Fig. 7C; (Jager et al., 2016; Paredes et al., 2016). This was plotted at a population level as frequency distribution using heat maps, for each nucleus individually, for E17.5 and P0.5 (Fig. 7D; Supp. Fig. 3B), as the relative increase in GFP$^+$ cell numbers was the greatest between these two timepoints (Fig. 7B). Moreover, there was a progressive decrease across developmental stages in the proportion of GFP$^+$ cells for which migratory morphology could be identified (Supp. Fig. 3A).

Heat maps indicate that at a population level (integrated across dimensions), GFP$^+$ cells migrate into the LGd, LP and VP in a caudo-rostral and dorso-ventral direction (Fig. 7D), consistent with the position of the thalamus in the brain relative to their midbrain origin. However, GFP$^+$ precursors in the LGd and LP have a dominant medio-lateral orientation, while those in the VP an opposite, latero-medial orientation, as can also be seen from polar histograms (Supp. Fig. 3C). This suggests that midbrain-derived interneuron precursors enter TC regions simultaneously in two distinct streams, one migrating rostro-ventro-laterally to the LGd and LP, and the other rostro-ventro-medially to the VP, indicating a split between visual (LGd, LP) and somatosensory (VP) TC nuclei.

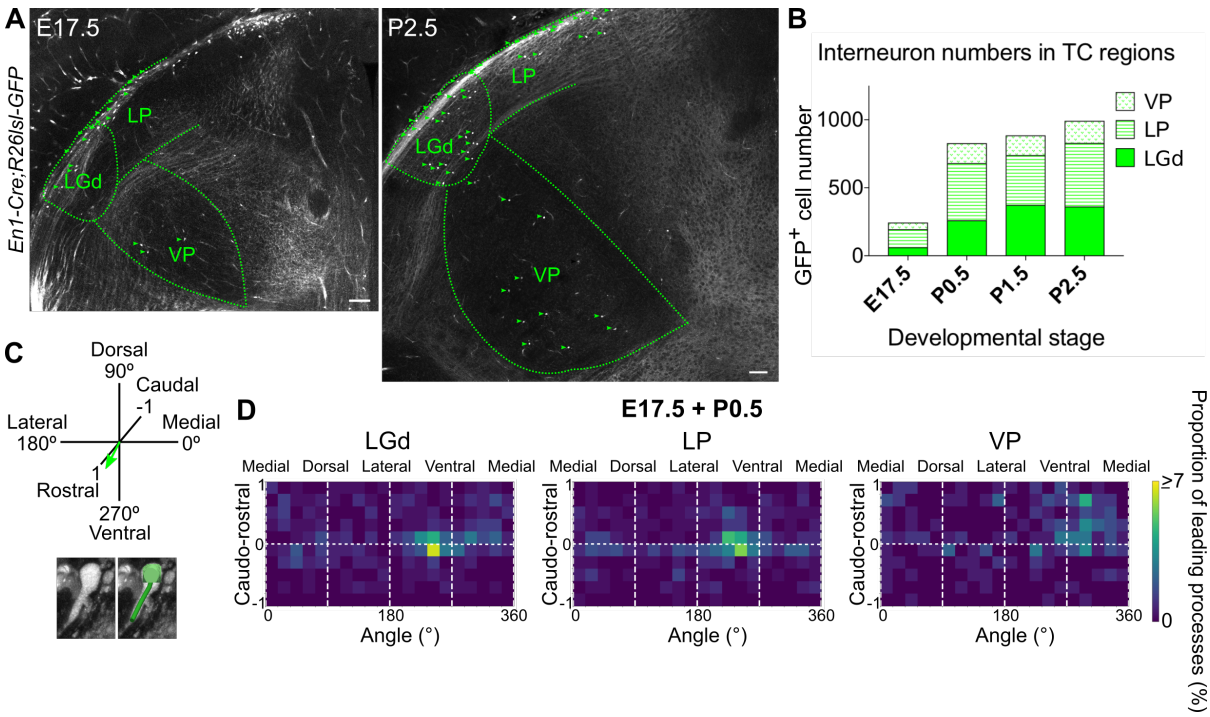

Figure 7. Midbrain-derived IN precursors progressively populate the thalamus from E17.5 onwards. A. Representative coronal sections of *En1-Cre;R26lsl-GFP* thalamus at E17.5 and P2.5. Green arrows mark some of the GFP$^+$ cells. Scale bars, 100µm. **B.** Number of GFP$^+$ cells counted in the LGd, LP and VP from E17.5 to P2.5 (mean, n=3 brains). **C.** Leading process orientation of GFP$^+$ cells was determined along the caudo-rostral, ventro-dorsal and latero-medial dimensions. **D.** Frequency distribution of leading process orientation for GFP$^+$ cells in the LGd, LP and VP at E17.5 and P0.5 combined, represented in heat maps (n=3 brains/developmental stage).

Sox14-negative thalamic interneurons populating higher order nuclei are born in the forebrain

Having excluded the midbrain, we aimed to identify the origin of the *Sox14*$^-$ interneuron class in the mouse. To molecularly define it, we made use of DropViz data [Available from: dropviz.org; (Saunders et al., 2018)] and observed that within inhibitory clusters from the diencephalon, *Sox14* and *Pvalb* show largely non-overlapping expression. It is known that *Pvalb* is expressed by the prethalamic RT (Clemente-Perez et al., 2017) and by telencephalic interneuron subtypes derived from the GE (Marín and Rubenstein, 2001; Tasic et al., 2016; Tremblay et al., 2016).

We therefore checked whether any thalamic interneurons are labelled by a *Pv-Cre* (Hippenmeyer et al., 2005) *R26lsl-nuclearGFP* (Mo et al., 2015) reporter line. Indeed, at P14 *nuclearGFP* was detected in GABA-expressing neurons within the same regions populated by the *Sox14*$^-$ interneurons (Supp. Fig. 5A), including the MD and LD, but absent from TC nuclei populated exclusively by *Sox14*$^+$ interneurons, such as the LGd and VP (Supp. Fig. 5Ai).

At later ages (P56) *Pvalb* is widely expressed in the mouse thalamus and is observed in high-density gradients in several TC nuclei (© 2004 Allen Institute for Brain Science. Allen Mouse

Brain Atlas. Available from: mouse.brain-map.org; (Lein et al., 2006). *Pvalb* expression is not conserved across rodents and primates and cannot assist in comparative studies (Rausell and Jones, 1991). Importantly however, in the P14 mouse 93.9% of *Pvalb*$^+$ cells in TC regions co-expressed GABA (n=2 brains, Supp. Fig. 5Aii,B). Therefore, we define the mouse *Sox14*$^-$ GABAergic cells as *Pvalb*$^+$.

We found the presence of a minor population of Pvalb$^+$ interneurons in the anterior thalamus of the mouse (see Fig. 3Bii and Supp. Fig. 2B) intriguing. Spatial proximity to the RT and shared marker expression (*Pvalb)*, may suggest a prethalamic origin. On the other hand, progenitor domains of the telencephalic medial ganglionic eminences (MGE) and preoptic area (POA) also generate *Pvalb*$^+$ interneurons, which are known to integrate in neocortical and hippocampal circuitries (Gelman et al., 2011; Lavdas et al., 1999; Wichterle et al., 2001; Xu et al., 2004; Xu et al., 2008), but could potentially reach the thalamus. In addition, in humans only, the *DLX1/2/5*$^+$ ganglionic eminences (GE) generate thalamic interneurons selectively for the HO MD and pulvinar nuclei (Letinić and Kostović, 1997; Letinic and Rakic, 2001; Rakić and Sidman, 1969).

We set out first to investigate whether any of these alterative forebrain sources contribute the rarer *Sox14*$^-$ inhibitory class by fate-mapping telencephalic and prethalamic inhibitory progenitor domains using the *Dlx5-Cre* (Monory et al., 2006) crossed to *R26lsl-GFP* line (Fig. 8A).

At P14 all TC Pvalb$^+$ cells are a *Dlx5* lineage (GFP$^+$; 100%, n=3 brains; Fig. 8B,Ei) and majority of them co-expressed detectable GABA (93.6±3.7%; Fig. 8Eii), in line with observations from the *Pv-Cre;R26lsl-nGFP* line (Supp. Fig. 5Aii,B).

We also observed other Pvalb$^-$*Dlx5*$^+$ cells in the thalamus, the majority of which had a glia-like morphology and did not express GABA (Supp. Fig. 5C). Occasional Pvalb$^-$GABA$^-$*Dlx5*$^+$ cells with neuronal-like morphology were also seen (Supp. Fig. 5C,D), suggesting leaky Cre activity in some cases. That all Pvalb$^+$*Dlx5*$^+$ cells in TC nuclei are labelled with GFP argues against this being an artefact of leaky reporting. Pvalb$^-$GABA$^-$*Dlx5*$^+$ cells were not considered in any of the analyses.

To further discriminate between GABAergic progenitors of the MGE (*Dlx5*$^+$*Nkx2.1*$^+$) and of the prethalamus (*Dlx5*$^+$*Nkx2.1*$^-$), we fate-mapped *Nkx2.1*$^+$ lineages by crossing *Nkx2.1-Cre* (Xu et al., 2008) to *R26lsl-GFP* line (Fig. 8C) and investigated the presence of GFP$^+$Pvalb$^+$ co-expressing neurons in TC regions, at P14. While GFP$^+$ cells are present in thalamic territory, none of the TC Pvalb$^+$ cells belonged to a *Nkx2.1*$^+$ lineage (GFP$^+$Pvalb$^+$ 0%, n=3 brains; Fig. 8D,Ei), suggesting that a forebrain *Dlx5*$^+$*Nkx2.1*$^-$ progenitor domain is the source of the *Pvalb*$^+$ thalamic interneurons.

Although we did not conduct a detailed investigation of cell types labelled by the *Nkx2.1-Cre*;*R26lsl-GFP* reporter in the thalamus, we noted several glia-like morphologies that were also negative for the pan-neuronal marker NeuN (data not shown).

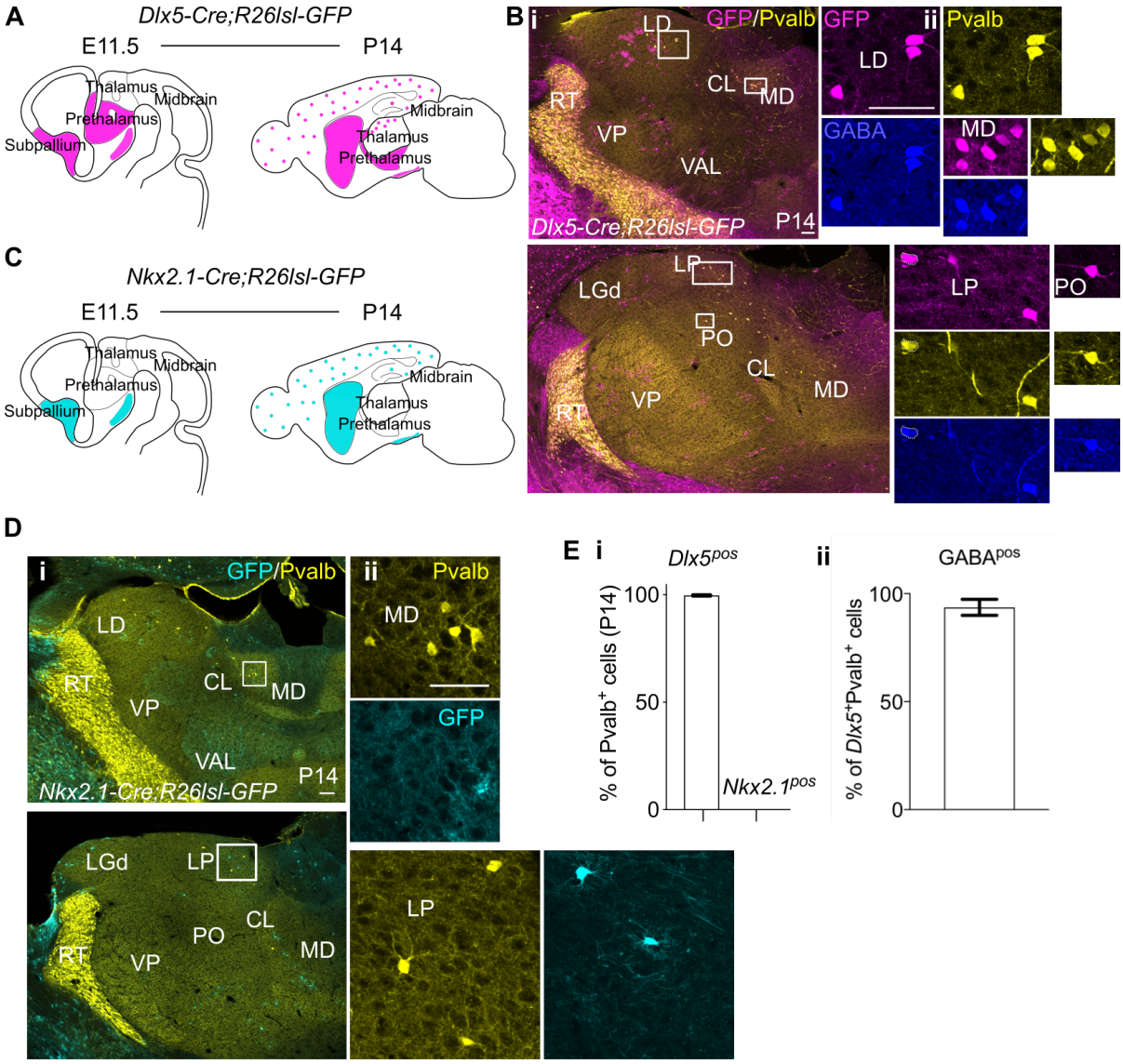

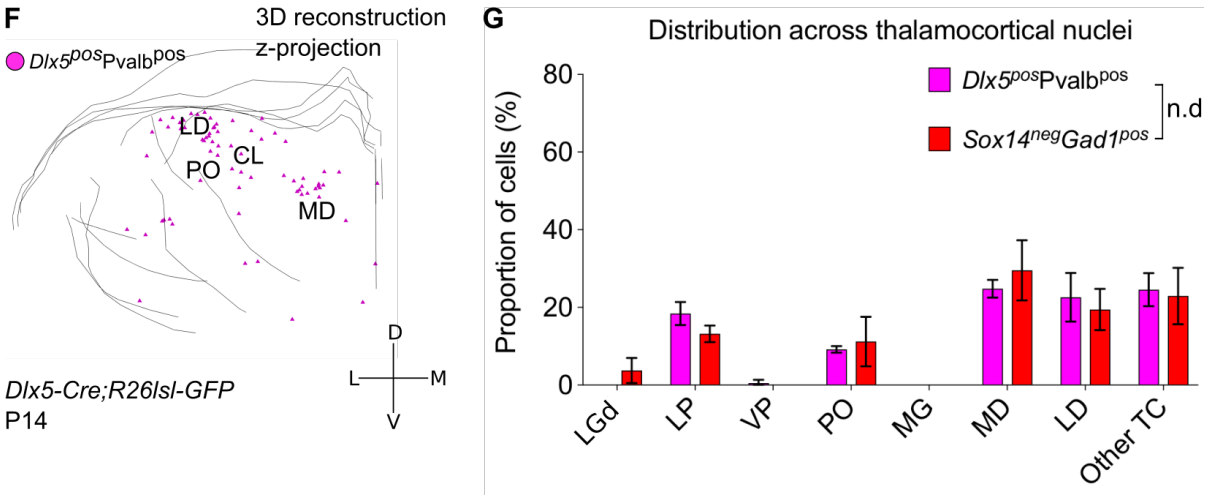

Figure 8. *Sox14*$^{-}$*Pvalb*$^{+}$ interneurons in TC regions derive from the *Nkx2.1*^{neg} rostral forebrain. A. Schematic of the fate mapping experiment: crossing *Dlx5-Cre* with *R26lsl-GFP* reporter line permanently labels some hypothalamic and all ventral telencephalic and prethalamic-born cells with GFP expression. **B.** (i) Representative coronal sections of P14 *Dlx5-Cre;R26lsl-GFP* thalamus with *Dlx5*$^{+}$Pvalb^{+} cells present in the MD, LD, CL, VAL, VM, LP and PO (considering TC regions only). Scale bar, 100µm. (ii) *Dlx5*$^{+}$Pvalb^{+} cells in TC regions co-express GABA. Scale bar, 100µm. **C**. Schematic of the fate mapping experiment: crossing *Nkx2.1-Cre* with *R26lsl-GFP* reporter line permanently labels some hypothalamic and all MGE-born cells with GFP expression. **D.** (i) Representative coronal sections of P14 *Nkx2.1-Cre;R26lsl-GFP* thalamus with Pvalb^{+} and *Nkx2.1*$^{+}$ cells present in the MD, LD, CL, VAL, VM, LP and PO (considering TC regions only). Scale bar, 100µm. (ii) *Nkx2.1*$^{+}$ cells in TC regions do not co-express Pvalb^{+}. Scale bar, 100µm. **E.** (i) Proportion of Pvalb^{+} cells in TC regions that are *Dlx5*$^{+}$ or *Nkx2.1*$^{+}$ at P14 (mean±SEM, n=3 brains). (ii) Proportion of *Dlx5*$^{+}$Pvalb^{+} cells in TC regions co-expressing GABA at P14 (mean±SEM, n=3 brains). **F.** 3D reconstruction of a representative P14 *Dlx5-Cre;R26lsl-GFP* thalamus from tracing every sixth 60µm-thick coronal section, displayed as a z-projection and showing distribution of *Dlx5*$^{+}$Pvalb^{+} cells. **G.** Distribution of *Dlx5*$^{+}$Pvalb^{+} and *Sox14*$^{-}$*Gad1*$^{+}$ cells across TC nuclei in P14 *Dlx5-Cre;R26lsl-GFP* and *Sox14*$^{GFP/+}$ brains, respectively, plotted as proportion of all the cells within each group (mean±SEM, n= 3 brains/genotype). The two populations are not differently distributed (p>0.05, Chi-squared test).

Finally, we mapped the distribution of Pvalb^{+}*Dlx5*$^{+}$ cells across TC regions (Fig. 8F,G) and observed that it closely recapitulates the distribution of *Sox14*$^{-}$*Gad1*$^{+}$ cells (Fig. 8G; p>0.05, Chi-squared test). Despite being a *Pvalb*$^{+}$*Dlx5*$^{+}$ lineage, these thalamic interneurons likely do not share the same origin of cortical *Pvalb*$^{+}$ interneurons. Altogether, we therefore conclude that the rarer *Sox14*$^{-}$ thalamic interneuron class is a distinct lineage compared to the larger, midbrain-born *Sox14*$^{+}$ thalamic interneuron class, which likely originates from the *Nkx2.1*$^{-}$*Dlx5*$^{+}$ prethalamic progenitor domain, rather than the telencephalic *Nkx2.1*$^{+}$*Dlx5*$^{+}$ MGE.

Discussion

Our study reveals a previously unappreciated complexity of GABAergic interneurons in the mouse TC nuclei, demonstrating that interneurons are not restricted to the FO visual thalamus, but present across modalities and hierarchical levels that including limbic structures.

We recognise two broad thalamic interneuron classes, defined by their origin in either the *En1*$^{+}$ midbrain or the *Nkx2.1*$^{-}$*Dlx5*$^{+}$ rostral forebrain. However, the two ontogenetic programs contribute differentially to interneuron numbers, with the midbrain-derived class overwhelmingly more abundant.

The midbrain-derived interneurons depend on the Sox14 transcription factor, a gene that we had previously implicated in LGd interneuron differentiation (Jager et al., 2016) and a known postmitotic marker for GABAergic subtype neurogenesis in the brainstem (Achim et al., 2013; Achim et al., 2014; Huisman et al., 2019; Prekop et al., 2018). Taking advantage of a *Sox14*^{GFP} mouse line, we now provide absolute numbers and standardised anatomical distribution of

this major class of interneurons across the entire thalamus, in the *Sox14*$^{GFP/+}$ C57Bl/6 genetic background.

Rather than representing a peculiarity of mice, the midbrain ontogenetic programme may be the dominant source of thalamic interneurons in larger-brained mammals, as suggested by the identification of *SOX14*$^{+}$*GAD1*$^{+}$ interneurons across virtually all TC nuclei in the interneuron-rich thalamus of the marmoset. Consistent with a conserved midbrain ontogeny of thalamic interneurons, Jones previously described late appearance of interneurons in the ferret and macaque thalamus, progressively from caudal towards rostral nuclei (Hayes et al., 2003; Jones, 2002). It can also be seen from the BrainSpan Atlas of the Developing Human Brain (BrainSpan Atlas of the Developing Human Brain; available from: www.brainspan.org; (Miller et al., 2014) that both *GAD1* and *SOX14* expression increase in the dorsal thalamus in the mid-prenatal period (from postconception week 16), which would be consistent with a migration of midbrain-born interneurons into these regions.
Interestingly, grafting experiments using chick and quail embryos demonstrated a potential for midbrain cells to populate retino-recipient nuclei in the chick diencephalon (Martinez and Alvarado-Mallart, 1989). The grafted midbrain cells were observed migrating tangentially at the surface of the diencephalon and seemingly through the host optic tract before invading the regions targeted by the retinal projections (Martinez and Alvarado-Mallart, 1989). The neurotransmitter identity of these migrating cells is unknown, but their midbrain origin and distribution across the thalamus resemble the mouse *Sox14*$^{+}$ interneurons, suggesting that in birds too, the largest cohort of interneurons is a midbrain lineage. Relatedly, lineage tracing in chick, using a retroviral library, indicated that clonally related siblings can populate both the diencephalon and mesencephalon (Golden and Cepko, 1996), in keeping with a revised model of evolutionary relationship of caudal diencephalon and midbrain (Albuixech-Crespo et al., 2017). The distribution of *Sox14*$^{+}$ interneurons observed in the mouse is similar to the one described in the opossum, a living marsupial thought to resemble early mammals in the fossil record (Penny et al., 1984). Intriguingly, rather than spreading throughout the nucleus, interneurons occupy the lateral subdivision of the LP in the adult opossum thalamus (Penny et al., 1984), reminiscent of the route taken by migrating midbrain-derived interneuron precursors in the developing mouse thalamus.

While the emerging picture points to a midbrain ontogeny for the largest fraction of thalamic interneurons, this is not sufficient to explain the overall developmental complexity of interneurons in the thalamus. In both the mouse and marmoset, we now report the presence of *Sox14*$^{-}$*Gad1*$^{+}$ interneurons with drastically more restricted distribution. In the mouse this

interneuron class is found enriched in HO TC nuclei (the non-specific MD and LD, but also sensory-related LP and PO). Similarly, in the marmoset *SOX14*$^{-}$*GAD1*$^{+}$ interneurons are also a minor class enriched in the HO nuclei MD and LD in the anterior portion of the thalamus. This specific distribution is intriguing as it may reflect the requirement in some associative nuclei for interneurons with unique functional properties that the larger midbrain-derived class cannot provide. Such hypothetical evolutionary drive is not dissimilar to the one previously proposed for some interneurons of the human thalamus, where ganglionic eminence-derived *DLX1/2*$^{+}$ interneurons were shown to migrate into associative nuclei MD and pulvinar (Letinić and Kostović, 1997; Letinic and Rakic, 2001; Rakić and Sidman, 1969).

While a dual midbrain and forebrain ontogeny of thalamic interneurons emerges as the conserved mammalian blueprint for thalamic interneuron organization, with the midbrain-derived class contributing the largest proportion of interneurons and the forebrain-derived class enriched in selected HO TC nuclei, species-specific differences also exist. In the mouse, midbrain- and forebrain-derived interneurons are spatially segregated along clear anatomical and functional subdivisions of the thalamus, in the marmoset, presumptive midbrain-derived interneurons expanded dramatically and are more broadly distributed. The forebrain-derived interneurons are not found in precisely the same set of associative TC nuclei across mouse and marmoset, while the forebrain-derived human lineage previously described is thought to be an evolutionary innovation that migrates into the thalamus from the GE along transient anatomical structures that are not present in rodents and non-human primates (Letinić and Kostović, 1997). Consistent with this, our data support a model whereby the mouse, and by extension the marmoset *Sox14*$^{-}$*Gad1*$^{+}$ interneurons are specified in the *Nkx2.1*$^{-}$*Dlx5*$^{+}$ prethalamus, rather than subpallium. Technical limitations make a detailed assessment of lineage descent in non-human primates and humans more challenging and whether humans retained the prethalamic interneuron class that we described here, is currently unknown. Further investigation of species-specific differences may provide important cues to trace the evolution of the mammalian thalamocortical system, using interneurons as the key to unravel their complexity.

Materials and Methods

Animals

Species	Designation	Source or reference	Identifiers	Additional information
Mus musculus	Sox14^{tm1Tmj} (Sox14eGFP)	Crone et al., 2008	MGI ID: 3836003	Maintained in the C57BL/6J (Charles River

				Laboratories) background
Mus musculus	En1-Cre	Kimmel et al., 2000; The Jackson Laboratory	Stock No: 007916 MGI ID: 2446434	C57BL/6J background
Mus musculus	Dlx5/6-Cre	Monory et al., 2006; The Jackson Laboratory	Stock No: 008199; MGI ID:3758328	C57BL/6J background
Mus musculus	B6 PV^{cre}	Hippenmeyer et al., 2005; The Jackson Laboratory	Stock No: 017320; MGI ID:3590684	C57BL/6J background
Mus musculus	Nkx2.1-Cre	Xu et al., 2008	Stock No: 008661 MGI: J:131144	C57BL/6J background
Mus musculus	RCE:loxP	Sousa et al., 2009; The Jackson Laboratory	MMRRC Stock No: 32037-JAX MGI:4412373	C57BL/6J background
Mus musculus	Gt(ROSA)26Sortm5(CAG-Sun1/sfGFP)Nat	Mo et al., 2015; The Jackson Laboratory	Stock No: 021039; MGI ID: 5443817	C57BL/6J background
Callithrix jacchus	WT	Colony at RIKEN RRD)	-	-

Table 1: Animal models used in the study.

The mice were housed in the animal facilities at King's College London under standard conditions on a 12h:12h dark/light cycle, with unrestricted access to water and food. Housing and experimental procedures were approved by the King's College London Ethical Committee and conformed to the regulations of the UK Home Office personal and project licences under the UK Animals (Scientific Procedures) 1986 Act. Both female and male mice were used in a randomised way across experiments. The morning when the vaginal plug was observed was designated as embryonic day (E) 0.5 and the day of birth as postnatal day (P) 0.5.

Callithrix jacchus

Total of 7 New World marmoset (C. jacchus) monkey were used in this study. All experiments were conducted in accordance with the guidelines approved by the RIKEN Institutional Animal Care (W2020-2-022).

Immunohistochemistry and *in situ* hybridization

Mice were transcardially perfused with 4% PFA and the brains dissected and postfixed in PFA at 4°C overnight, then washed in PBS for at least 24 hours at 4°C. For *in situ* hybridization (ISH), brains were stored in PFA for 5 days, to minimise RNA degradation, and all the subsequent solutions were treated with diethyl pyrocarbonate (DEPC; AppliChem). The brains were cryoprotected in a sucrose gradient (10–20– 30%), frozen on dry ice and cryosectioned

as 20µm coronal sections collected on Superfrost Ultra Plus slides (Thermo Scientific) for ISH, or as 60µm free-floating coronal sections for IHC.

Immunohistochemistry

Antibody	Dilution	Incubation time	Source
Rabbit anti-GABA	1:2000	2X ON, 4ºC	Sigma, A2052
Chicken anti-Gfp	1:5000	2X ON, 4ºC	Abcam, Ab13970
Mouse anti-Parvalbumin	1:2000	1X ON, 4ºC	Sigma-Aldrich, P3088
Goat anti-chicken Alexa-488	1:500	2h, RT	Invitrogen, A11039
Goat anti-rabbit Alexa-568	1:500	2h, RT	Invitrogen, A11036
Goat anti-rabbit Alexa-647	1:500	2h, RT	Invitrogen, A21245
Goat anti-mouse Alexa-568	1:500	2h, RT	Invitrogen, A11004
Goat anti-mouse Alexa-635	1:500	2h, RT	Invitrogen, A31575

Table 2: Antibodies

Brain sections were washed in PBS three times and blocked in 2-7% normal goat serum (NGS) solution (in 1X PBS, 0.1-0.3% Triton-X100) for 2 hours at room temperature (RT). Primary antibodies (Table 2) were diluted in blocking solution and incubated with the sections (as stated in the table). This was followed by three 30min PBS washes, and incubation in secondary antibodies (Table 2) diluted 1:500 in blocking solution, for 2 hours at RT. After two 30min PBS washes, the sections were incubated in DAPI for 30 min (1:40000 dilution in PBS; Life Technologies), and mounted using ProLong Gold mounting media (Invitrogen).

In situ hybridization

Gad1 antisense RNA probe was transcribed *in vitro* from full-length cDNA template (IMAGE ID: 5358787). The probe was diluted to a final concentration of 800ng/ml in hybridization buffer (50% formamide, 10% dextran sulphate, 1mg/ml rRNA, 1X Denhardt's solution, 0.2M NaCl, 10mM Tris HCl, 5mM $NaH_2PO_4.2H_2O$, 1mM Tris base, 50mM EDTA) and applied onto the slides, which were incubated in a humidified chamber at 65°C overnight. The slides were then washed three times for 30min in wash buffer (50% formamide, 1X SSC, 0.1% Tween) at 65°C, two times for 30min in MABT buffer (100mM maleic acid, 150mM NaCl, 0.1% Tween-20) at RT, and blocked for 2h at RT (2% Boehringer Blocking Reagent (Roche), 20% inactivated sheep serum in MABT). Sheep a-DIG alkaline phosphatase conjugated antibody (Roche, 11093274910) was diluted 1:2000 in the blocking solution and incubated with the slides overnight at 4°C. This was followed by five 20min washes in MABT and two 20min washes in the AP buffer (0.1M Tris-HCl pH8.2, 0.1%-Tween-20). Fast red TR/Naphthol AS-MX tablets (Sigma) were dissolved in the AP buffer and applied onto the slides for colour reaction for 3–6 hours at RT in the dark. The slides were then washed three times for 20min in PBS before proceeding with IHC for GFP as described above. *Sox14*$^{GFP/+}$ and *Sox14*$^{GFP/GFP}$ sections were always processed in parallel.

In situ hybridisation in Callithrix jacchus

Fluorescent in situ hybridization was performed as previously described (Watakabe et al.,

2006) with some modifications. Riboprobes incorporating digoxigenin- (DIG) and fluorescein- (FL) were hybridized overnight. After washing, FL- and DIG-labelled probes were each detected in different ways. For detection of the DIG probes, the sections were incubated with an anti-DIG antibody conjugated with horse radish peroxidase (HRP) (1/500, Roche Diagnostics) for 6 hours at room temperature. After washing in TNTx (0.1 M Tris-HCl, pH 7.5, 0.15 M NaCl, 0.05% Triton X-100) three times for 5 minutes, the sections were treated with 1:100 diluted TSA-Plus (DNP) reagents (Perkin Elmer) for 20 minutes. After washing in TNTx 3 X 10 minutes, the sections were incubated for 2 hours at room temperature with an anti-DNP antibody conjugated with Alexa 488 (1/500, Invitrogen). After quenching HRP activity and washing, the sections were incubated for 2 hours at room temperature with an anti-FL antibody conjugated with HRP (1/500, Roche Diagnostics) followed by reaction with TSA biotin reagents (Perkin Elmer) and visualization with streptavidin conjugated with Alexa594 (Invitrogen).

Quantifying distribution of neuronal populations in histological sections

In mice. Confocal z-stacks covering the extent of the thalamus across all axes (caudo-rostral, ventro-dorsal, latero-medial) were acquired using either Nikon A1R inverted confocal, inverted spinning disk Nikon Ti microscope or Olympus VS120 slide scanner, with 10X (NA 0.30 Plan Fluor DLL) and 20X (NA 0.75 Plan Apo VC or UPLSAPO NA 0.75) objectives. The stacks were then viewed with the Neurolucida software. TC nuclei were identified from the DAPI counterstain, using cytoarchitectonically recognizable structures, such as the LGd, the habenular complex, the RT, the anterior pretectum and the fasciculus retroflexus (fr), as landmarks for orientation and reference. The cells of interest (Table 3) were assigned to TC regions by comparing the sections to the Allen Brain Reference Atlas and annotated and counted manually. For each brain, only one hemisphere was analysed (chosen in a randomized way). For experiments using *Gad1*$^{+}$ and *Chrna6*$^{+}$ *in situ* hybridization data from the Allen Mouse Brain Atlas resource (© 2004 Allen Institute for Brain Science. Allen Mouse Brain Atlas. Available from: mouse.brain-map.org; (Lein et al., 2006), all images of P56 C57BL/6J coronal brain sections containing the thalamus were downloaded for each gene (every 8th 25µm-thick section, sampling every 200µm across the thalamus), and analysed in the same way as described above.

In marmoset. Images were acquired with a fluorescence microscope BZ-X810 (Keyence) or BZ-9000 (Keyence). Representative coronal sections at anterior, intermediate and posterior levels were analysed manually, by delineating nuclear boundaries according to the neonate Marmoset Gene Atlas, RIKEN CBS, Japan (https://gene-atlas.brainminds.riken.jp). Cell counting was conducted using the Cell Counter Plugin and ROI manager in ImageJ (Schindelin et al., 2015). Within the boundaries of each TC nucleus analysed, 3 ROIs of

263μm by 263μm were positioned randomly and their content of single positive or double positive cells added together to generate a representative fraction of *GAD1*$^+$ and *GAD1*$^+$*SOX14*$^+$ cells for the TC nucleus (no SOX14 single positive cells were detected). Counts were replicated in 3 age matched brains to calculate mean±SEM.

Transgenic line	Age	Cells annotated/counted	Number of brains	Sampling	Section thickness (μm)
Mouse					
Sox14$^{GFP/+}$	P21	GFP$^+$	3	Whole thalamus	50 (10; optical sections)
Sox14$^{GFP/+}$	P14	GFP$^+$ and *Gad1*$^+$	3	Every 10th coronal section	20
Sox14$^{GFP/GFP}$	P14	GFP$^+$ and *Gad1*$^+$	3	Every 10th coronal section	20
En1-Cre;R26lsl-GFP	P21-30	GFP$^+$	3	Every 6th coronal section	60
Dlx5/6-Cre;R26lsl-GFP	P14	GFP$^+$, Pvalb$^+$ and GABA$^+$	3	Every 6th coronal section	60
Nkx2.1-Cre;R26lsl-GFP	P14	GFP$^+$, Pvalb$^+$	3	Every 6th coronal section	60
Pv-Cre;R26lsl-nGFP	P14	GFP$^+$, Pvalb$^+$ and GABA$^+$	2	Every 6th coronal section	60
Marmoset					
Wild type	P0	*SOX14* and *GAD1*	3	representative anterior, intermediate and posteorior planes	28

Table 3. Genetic identity of cells counted across TC regions and technical details of corresponding experiments.

3D reconstructions of cell distributions from histological sections

3D reconstructions of cell distributions (Table 3) across thalamic regions were generated for each brain separately using the Neurolucida software (MBF Bioscience), from the acquired confocal z-stacks or Allen Mouse Brain Atlas *in situ* hybridization data as described above. For each image the outline of the thalamus and the surrounding structures was manually traced using the 'contour' function and the cells were annotated with the 'marker' function, placed at the centre of the soma. Traced images were then aligned in sequential rostro-caudal order, manually for each brain, using tissue landmarks (midline and clearly recognisable structures, e.g. LGd, RT, habenula, hippocampus) for reference, and their spacing in the rostro-caudal dimension was preserved according to the sampling used for each brain.

3D reconstructions of cell distributions by whole brain serial two photon imaging

Sox14$^{GFP/+}$ mouse brain samples (n=3) were embedded in a 4.5% oxidised-agarose solution containing agarose (type 1; Sigma), 10 mM NaIO4 (Sigma) and 50 mM phosphate buffer (PB).

Samples were imaged with TissueCyte 1000 (Ragan et al., 2012) with a custom cooling system (JULABO UK Ltd.) for serial two-photon (STP) tomography across the complete mouse brain. Physical sectioning was performed every 50 μm with optical sectioning every 10 μm. A 16x, 0.8 NA immersion objective (Nikon Inc.) acquired 1 × 1 mm image tiles at spatial resolution 0.54 μm with a 12 × 10 tiling mosaic required to obtain a complete coronal tissue section. Laser (Chameleon Ultra II, Coherent) excitation was conducted at 920 nm for GFP excitation with three PMT channel acquisition for red, green and blue wavelength collection. STP imaging occurred over 5 days and generated 3.5 terabytes of data per brain. Tiled data was stitched alongside STP acquisition using a custom Python and ImageJ/Fiji pipeline.

STP data sets of each mouse brain were down-sampled to 10 μm isotropic voxel size and registered with the Allen Common Coordinate Framework (CCF3) average atlas using Elastix (Klein et al., 2010). Registration was performed from average atlas (moving) to down-sampled STP (fixed) using a combination of rigid, affine and b-spline transformation steps, executed using a multiresolution approach for robust global and local structure registration. An advanced Mattes Mutual Information similarity metric and an adaptive stochastic gradient descent objective optimiser was used at each transformation step with the transformation at each step combined into a final transformation map which was applied to the CCF3 annotation atlas and a custom hemisphere atlas used to distinguish structures across hemisphere. Registration resulted in a spatial mapping from the STP data to the CCF3 atlas space allowing the delineation of thousands of anatomical structures according to the Allen Brain Atlas hierarchically organized taxonomy.

For automated cell counting, a U-Net (Ronneberger O., 2015) deep learning network was trained to segment fluorescently labelled cells in STP and confocal data sets. During training, 219 images of fluorescently labelled cells (512 × 512 pixels; 0.54 μm voxel size) were manually segmented using ImageJ/Fiji. Images came from STP and confocal data sets of GFP labelled cells from transgenic mouse lines and viral tracing studies and contained GFP expression localised to soma and dendritic and axonal structures. During manual segmentation, only soma localised fluorescence was labelled. To increase generalisation of the network for robust performance on new data, drop out layers at 50% probability were introduced into the network, plus image augmentation was used to increase the initial 219 image data set by 56-fold. Augmentation operations included image flipping, rotation in the range -360° to +360°, zooming in the range 90% to 110%, skewing, a random elastic distortion using a grid size of 10 pixel spacing, shearing and a custom Poisson noise addition. Some transformations were assisted using the Python package Augmentor (D' Bloice, 2017), with the custom Poisson

noise generation written as a class to interface with the Augmentor package. Each transformation was given a 50% probability of occurring and resulted in a final training data set of 12,264 image and annotated pairs. Training data was split 75% (9,198 samples) for training the network and 25% (3,066 samples) for validating the network with conscious effort to maintain class balance between the training and validation to prevent overfitting or loss issues during training.

The model was trained with the ELU activation function, using an Adam optimiser with a Binary Cross-entropy loss function. A batch size of 8 was used with early stopping evoked if a validation dice loss score did not improve after 30 epochs of training. Model training was performed on a workstation equipped with a NVIDIA Titan Xp GPU using Python and the TensorFlow 2.0 platform.

For automated thalamus counting, all structures belonging to the thalamus, according to the Allen Brain Atlas hierarchically organized taxonomy, were extracted from the registered STP data sets using masks upsampled to the original 0.54 µm data and fed into the trained network for automated segmentation. Correction for oversampling of cells in the axial axis was done by grouping detected cells if they overlapped within a radius of 10 µm, and subsequently keeping the centrally positioned cell in the axial axis. Automated counting in the entire thalamus took 7 hours per sample using an Ubuntu Intel(R) Core(TM) i9-7980XE CPU at 2.60GHz workstation, with 32 cores and 128 GB RAM.

Nearest Neighbour Distance calculations

Nearest neighbour distance (NND) was determined for the *Sox14*$^{+}$*Gad1*$^{+}$ and *Sox14*$^{-}$*Gad1*$^{+}$ cells from the 3D reconstructions of their distributions. The cells' coordinates in 3D were generated by Neurolucida and analysed using a custom Python script and the Pandas library (McKinney, 2010) to calculate NNDs separately for each group and between the two groups, for each *Sox14*$^{GFP/+}$ brain individually. The data was then normalised to the largest NND within each data set (each individual group and between groups sets for each brain), averaged across the brains (mean±SEM) and plotted as cumulative distribution. Normalization allows us to plot their cumulative distribution as a fraction of the maximum distance, though even before normalization the curves were broadly similar. Statistically significant differences between the distributions were verified using the 2-sample Kolmogorov-Smirnov test, implemented in the SciPy library (Jones et al.).

Migratory morphology analysis

E16.5, E17.5, P0.5, P1.5 (n=3 brains/developmental stage) and P2.5 (n=1) *En1-Cre;R26lsl-GFP* brains were quickly dissected on ice and immersed in 4% PFA for 12 hours before switching to PBS. 300µm-thick coronal sections were cut on a vibratome (Leica VT 1200S). To increase the imaging depth, the sections were cleared following the ScaleSQ protocol (Hama et al., 2015). ScaleS4 buffer was used as a mounting medium (Hama et al., 2015), and spacers were placed on the slides to prevent compressing the sections. Nikon A1R inverted confocal was used to acquire z-stacks that covered the entire extent of the thalamus for each brain, with a 20X objective (NA 0.75 Plan Apo VC). The achieved imaging depth in *z* ranged from 200-250µm. The stacks were imported into Neurolucida software (MBF Bioscience) to trace the migratory morphology of GFP^+ cells in the LGd, LP and VP. On average, 2 sections covered the extent of these nuclei in the rostro-caudal dimension and the first time point when GFP^+ cells were observed there was at E17.5. GFP^+ cells were not traced in the PO and MG due to their low numbers in these nuclei in the juvenile and adult brains, and the ambiguity in delineating these regions anatomically in the embryonic brains. We did not observe GFP^+ cells with neuronal morphology in any other TC regions (i.e. outside the FO and HO sensory thalamus) for all ages analysed. In the analysed regions (LGd, LP, VP), all GFP^+ somas were annotated using the semi-automated 'Soma' function. The leading processes were traced manually with the 'Tree' function, starting in the middle of the soma and until each process could be unequivocally identified or until the point of bifurcation, for all GFP^+ cells with a clearly visible and identifiable leading process (44% of all GFP^+ cells at E17.5, 30% at P0.5, 26% at P1.5, 14% at P2.5). The 3D coordinates for each leading process were then exported into Excel, and their orientation was expressed in the brain's coordinate system (x=L-M, y=V-M, z=C-R), as a vector joining the start and end point of the process, using a custom Python script and the Pandas (McKinney, 2010) and Numpy (Walt et al., 2011) libraries. Each vector was defined by its orientation in spherical coordinates (polar and azimuthal angle), and overall length. Population level orientation data for the LGd, LP and VP at E17.5 and P0 was plotted as heat-maps, by binning cells according to their spherical coordinates. The bins were then integrated along each axis to reveal a dominant orientation (e.g. for the LGd, 66% and 69% of cells oriented dorso-ventrally and caudo-rostrally, respectively). Polar histograms of leading process orientation in the dorsal-ventral-lateral-medial plane were also produced.

Spatial clustering analysis

Unsupervised machine learning methods were used to investigate spatial organization of *Sox14*$^+$*Gad1*$^+$ and *Sox14*$^-$*Gad1*$^+$ cells. The 3D models of P14 *Sox14*$^{GFP/+}$ thalamus generated with Neurolucida for NND analysis were again used to obtain the coordinates of all thalamic interneurons.

These data were analysed separately for each brain (n=3) using a custom Python script, and partitioned into clusters using the k-Means algorithm implemented in the library Scikit-Learn (Buitinck et al., 2013). The algorithm takes as input the expected number of clusters *k*.
Multiple values of *k* were tested, and evaluated using the silhouette coefficient metric of clustering performance (Rousseeuw, 1987), also implemented in Scikit-Learn. The silhouette coefficient is equal to the average ratio of distances between points within and between each cluster. More positive scores indicate coherent, well-separated clusters, whereas scores close to zero indicate overlapping clusters. The score was highest (0.472±0.012) for k=2, and the average fraction of all *Sox14*$^{+}$ and *Sox14*$^{-}$ cells in each of the resulting clusters was computed across all brains.
We also performed k-Means clustering on the 3D distribution of *Gad1*$^{+}$ cells obtained from *in situ* hybridisation data from the Allen Mouse Brain Atlas. The silhouette score was again highest (0.512) for k=2, and the resulting clusters have a spatial definition similar to those from the P14 *Sox14*$^{GFP/+}$ thalamus.

Statistics

Comparison of distributions

The Chi-squared test was used to test for significant differences in the thalamus-wide distribution of specific cell classes. This thalamus-wide comparison compensates for categorical errors arising from a degree of uncertainty in nuclear boundaries, as a result of variation in the sectioning plane and other factors.
For each distribution, average relative cell numbers were computed in Excel. A custom python script was used to compute the Chi-squared statistic, and the corresponding p-value was computed using the Chi-squared cumulative density function implemented in SciPy (Jones et al.).

Change in interneuron numbers in the Sox14 knockout

This was tested for statistical significance using unpaired two-sample two-tailed t-test, comparing the *Sox14* knockout to *Sox14*$^{GFP/+}$ for each interneuron class separately (n=3 brains/genotype). Total interneuron numbers across all TC nuclei were compared and sampling was consistent between genotypes (each 10th thalamic section was analysed for each brain).
Other statistical analyses used in the study are described in the corresponding sections (Nearest Neighbour Distance calculations and Spatial clustering analysis).

Identification of outliers

The fraction of GAD1 single positive cells is low across all in most TC nuclei tested, this low frequency is partly due to the lower efficiency of the SOX14 probe compared to the GAD1 and

therefore a systematic error. In the LD and MD, however, the frequency of GAD1 single positive is higher. To demonstrate that values for these two TC nuclei are outliers, we applied the method described in (Motulsky and Brown, 2006), implemented in GraphPad Prism software.

Acknowledgments

We thank the Wohl Cellular Imaging Centre, King's College London for support with imaging and image analysis software. We are grateful to Beatriz Rico and Patricia Hernandez at King's College London for the *Nkx2.1-cre;R26lsl-GFP* samples. This work was funded by the Biotechnology and Biological Sciences Research Council (BBSRC) grants BB/L020068/1 and BB/R007020/1 to A.D.

Author Contributions

Conceptualization: P.J. and A.D.; Investigation and analysis: P.J., G.M., P.C., X.D., I.S., Y.K., Y.W. and A.D.; Resources: S.S., S.B., T.S. and A.D.; Writing: P.J. and A.D.

Competing Interests

The authors declare no competing interests.

Supplementary Material

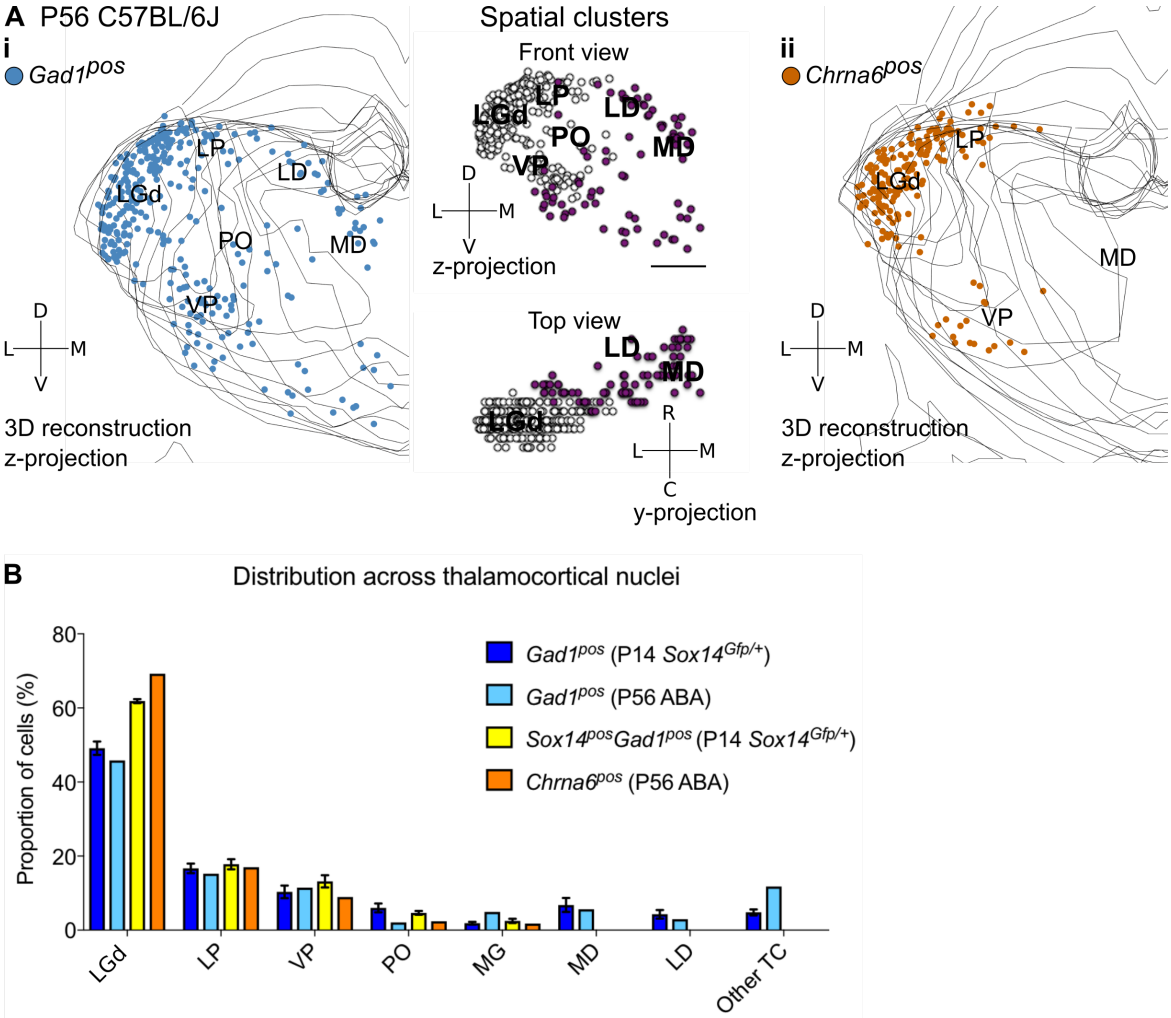

Supplementary Figure 1. A. 3D reconstruction of a representative P56 mouse thalamus from tracing every eight 25µm-thick coronal section, displayed as a z-projection and showing distribution of (i) *Gad1*$^{+}$ and (ii) *Chrna6*$^{+}$ cells. In (i), k-Means clustering was applied to the data using k=2 (highest silhouette score, 0.512); the resulting spatial clusters are shown as a z- and y-projection and colour-coded. One dot represents one neuron. ISH data was downloaded from the Allen Mouse Brain Atlas (© 2004 Allen Institute for Brain Science. Allen Mouse Brain Atlas. Available from: mouse.brain-map.org; Lein et al., 2006). **B.** Distribution of *Gad1*$^{+}$ and *Chrna6*$^{+}$ cells across TC nuclei (n=1 brain/marker) is compared to all *Gad1*$^{+}$ and *Sox14*$^{+}$*Gad1*$^{+}$ cells from P14 *Sox14*$^{GFP/+}$ thalamus (n=3 brains; see also Fig. 2).

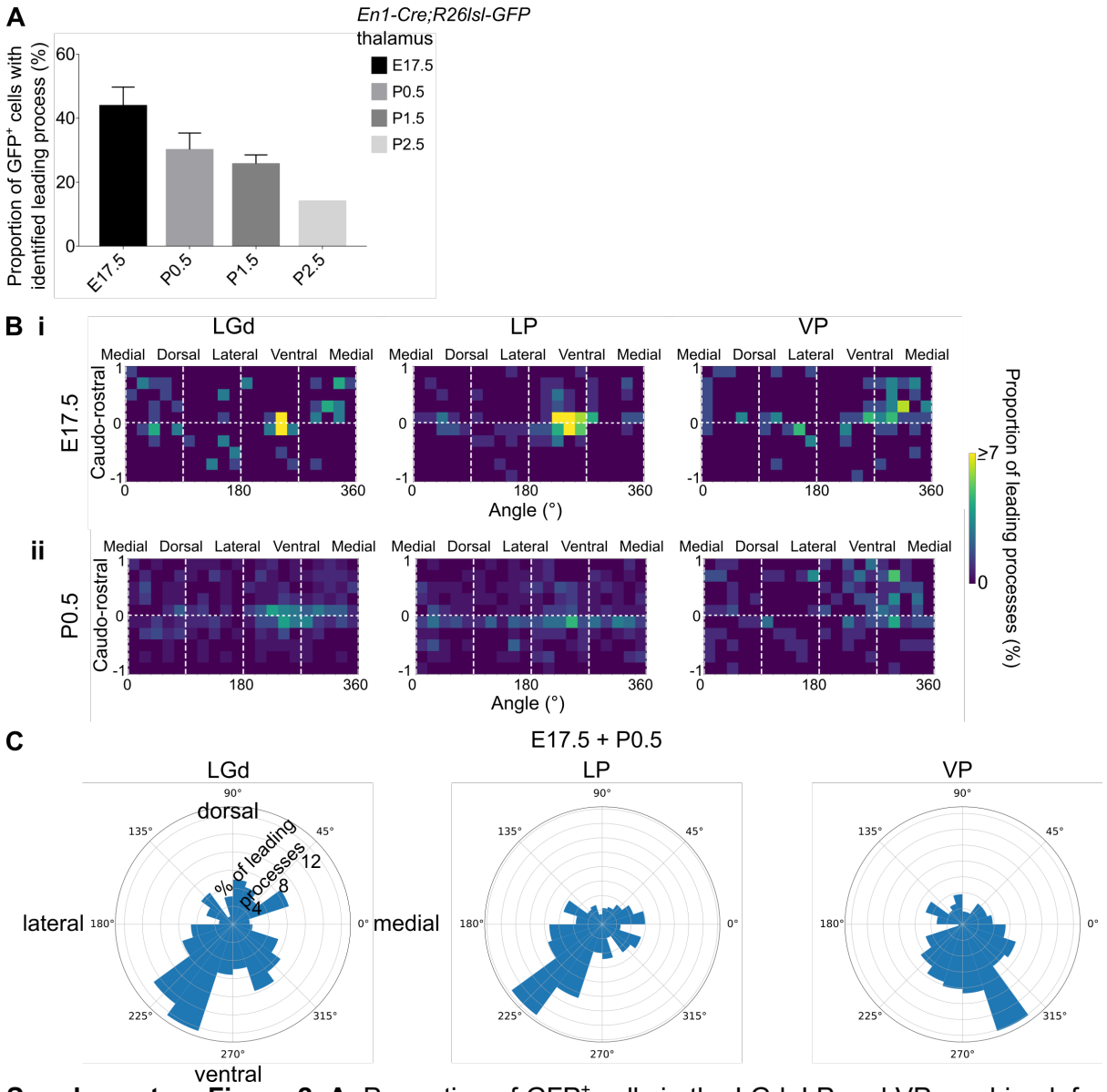

Supplementary Figure 2. A. Proportion of GFP$^+$ cells in the LGd, LP and VP combined, for which a leading process could be identified, in E17.5-P2.5 *En1-Cre;R26lsl-GFP* brains (mean±SEM, n=3 brains/developmental stage, apart from P2.5 where n=1 brain). **B.** Frequency distribution of leading process orientation for GFP$^+$ cells in the LGd, LP and VP at (i) E17.5 and (ii) P0.5 separately, represented in heat maps (n=3 brains/developmental stage). **C.** Polar histograms of leading process orientation in the latero-medial and ventro-dorsal plane for GFP$^+$ cells in the LGd, LP and VP at E17.5 and P0 combined (n=3 brains/developmental stage).

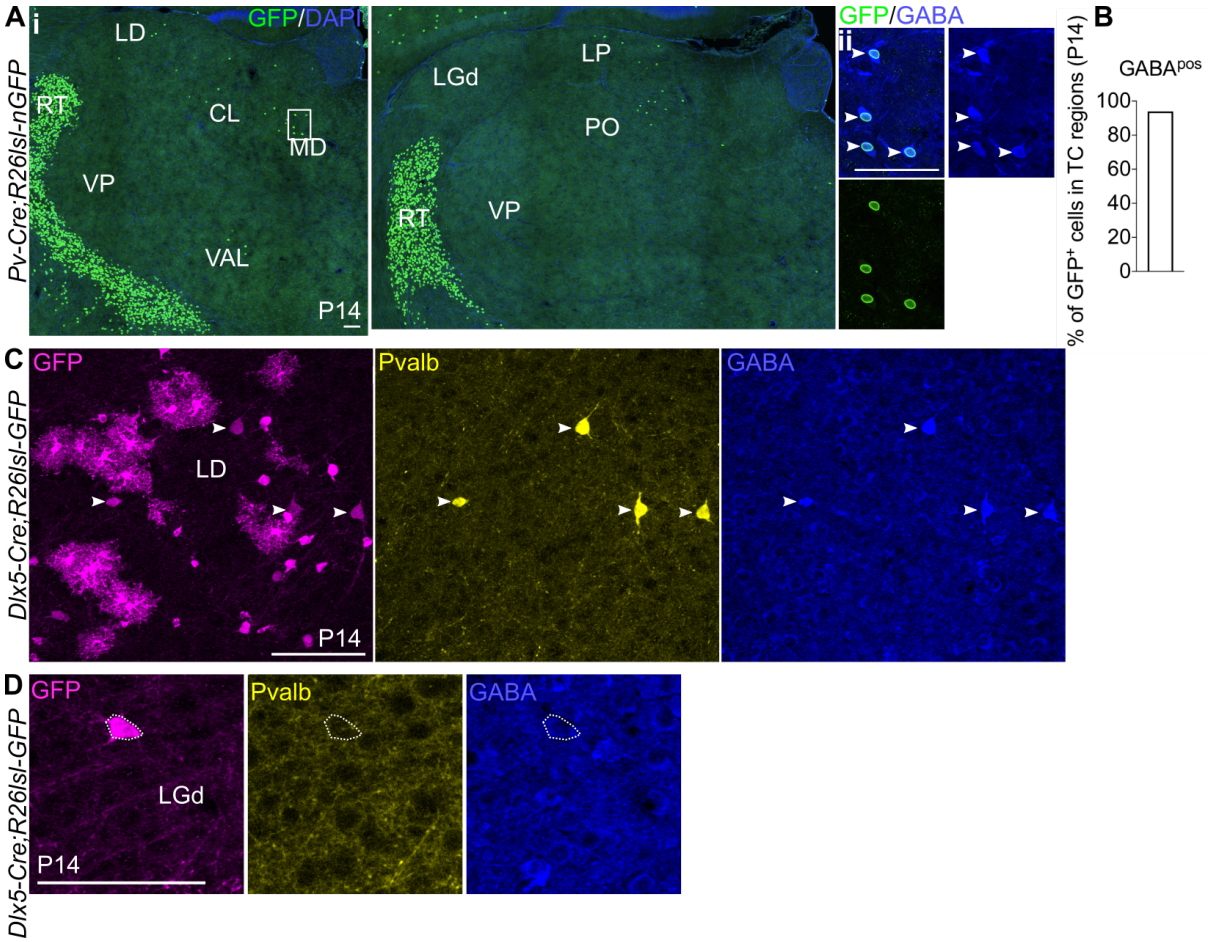

Supplementary Figure 3. A. (i) Representative coronal sections of P14 *Pv-Cre;R26lsl-nGFP* thalamus with GFP$^+$ cells present in the MD, LD, CL, VAL, LP and PO (considering TC regions only). Scale bar, 100µm. (ii) GFP$^+$ cells in TC regions express GABA at P14. Scale bar, 100µm. **B.** Proportion of GFP$^+$ cells in TC regions co-expressing GABA at P14 (mean, n=2 brains). **C.** Clusters of Pvalb$^-$GABA$^-$*Dlx5*$^+$ glia-like cells are observed across TC regions in the *Dlx5-Cre;R26lsl-GFP* line at P14, as shown for the LD. White arrows mark Pvalb$^+$GABA$^+$*Dlx5*$^+$ cells. Scale bar, 100µm. **D.** Pvalb$^-$*Dlx5*$^+$ cells with neuronal morphology do not express GABA. Scale bar, 100µm.

Supplementary Movie 1. A video animation of 28 z-stacks (each 100 µm) of projected coronal slices, downsized to 1 um voxel size in XY to reduce file size. Each slice is a maximum intensity projection across 10 serial two-photon optical slices.

Supplementary Movie 2. A video animation of the anatomical delineations from the Allen Institute Common Coordinate Framework (CCF3) projected onto the imaging data from a P21 *Sox14*$^{GFP/+}$ brain. Isotropic 10 µm voxel size.

References

Achim, K., Peltopuro, P., Lahti, L., Tsai, H.-H., Zachariah, A., Astrand, M., Salminen, M., Rowitch, D., and Partanen, J. (2013). The role of Tal2 and Tal1 in the differentiation of midbrain GABAergic neuron precursors. In Biology Open (Company of Biologists), pp. 990-997.

Achim, K., Salminen, M., and Partanen, J. (2014). Mechanisms regulating GABAergic neuron development. In Cellular and Molecular Life Sciences, pp. 1395-1415.

Albuixech-Crespo, B., Lopez-Blanch, L., Burguera, D., Maeso, I., Sanchez-Arrones, L., Moreno-Bravo, J.A., Somorjai, I., Pascual-Anaya, J., Puelles, E., Bovolenta, P.*, et al.* (2017). Molecular regionalization of the developing amphioxus neural tube challenges major partitions of the vertebrate brain. PLoS Biol *15*, e2001573.

Arcelli, P., Frassoni, C., Regondi, M.C., De Biasi, S., and Spreafico, R. (1997). GABAergic neurons in mammalian thalamus: a marker of thalamic complexity? In Brain research bulletin, pp. 27-37.

Arendt, D., Bertucci, P.Y., Achim, K., and Musser, J.M. (2019). Evolution of neuronal types and families. In Current Opinion in Neurobiology, pp. 144-152.

Armstrong, E. (1979). A quantitative comparison of the hominoid thalamus. I. Specific sensory relay nuclei. In American Journal of Physical Anthropology (John Wiley & Sons, Ltd), pp. 365-381.

Baldwin, M.K.L., Balaram, P., and Kaas, J.H. (2017). The evolution and functions of nuclei of the visual pulvinar in primates. In Journal of Comparative Neurology (John Wiley & Sons, Ltd), pp. 3207-3226.

Bickford, M.E., Slusarczyk, A., Dilger, E.K., Krahe, T.E., Kucuk, C., and Guido, W. (2010). Synaptic development of the mouse dorsal lateral geniculate nucleus. In Journal of Comparative Neurology (Wiley Subscription Services, Inc., A Wiley Company), pp. 622-635.

Bickford, M.E., Wei, H., Eisenback, M.A., Chomsung, R.D., Slusarczyk, A.S., and Dankowsi, A.B. (2008). Synaptic organization of thalamocortical axon collaterals in the perigeniculate nucleus and dorsal lateral geniculate nucleus. In The Journal of comparative neurology, pp. 264-285.

Bolkan, S.S., Stujenske, J.M., Parnaudeau, S., Spellman, T.J., Rauffenbart, C., Abbas, A.I., Harris, A.Z., Gordon, J.A., and Kellendonk, C. (2017). Thalamic projections sustain prefrontal activity during working memory maintenance. In Nature Neuroscience (Nature Publishing Group, a division of Macmillan Publishers Limited. All Rights Reserved.), pp. 987.

Braak, H., and Bachmann, A. (1985). The percentage of projection neurons and interneurons in the human lateral geniculate nucleus. In Human neurobiology, pp. 91-95.

Buitinck, L., Louppe, G., Blondel, M., Pedregosa, F., Mueller, A., Grisel, O., Niculae, V., Prettenhofer, P., Gramfort, A., Grobler, J.*, et al.* (2013). API design for machine learning software: experiences from the scikit-learn project. In ECML PKDD Workshop: Languages for Data Mining and Machine Learning, pp. 108-122.

Butler, A.B. (2008). Evolution of the thalamus: a morphological and functional review. In Thalamus & Related Systems (Cambridge University Press), pp. 35-58.

Cheong, S.K., Tailby, C., Solomon, S.G., and Martin, P.R. (2013). Cortical-Like Receptive Fields in the Lateral Geniculate Nucleus of Marmoset Monkeys. In The Journal of Neuroscience, pp. 6864 LP - 6876.

Clascá, F., Rubio-Garrido, P., and Jabaudon, D. (2012). Unveiling the diversity of thalamocortical neuron subtypes. In European Journal of Neuroscience, pp. 1524-1532.

Clemente-Perez, A., Makinson, S.R., Higashikubo, B., Brovarney, S., Cho, F.S., Urry, A., Holden, S.S., Wimer, M., Dávid, C., Fenno, L.E.*, et al.* (2017). Distinct Thalamic Reticular Cell Types Differentially Modulate Normal and Pathological Cortical Rhythms. In Cell Reports, pp. 2130-2142.

Crone, S.A., Quinlan, K.A., Zagoraiou, L., Droho, S., Restrepo, C.E., Lundfald, L., Endo, T., Setlak, J., Jessell, T.M., Kiehn, O.*, et al.* (2008). Genetic ablation of V2a ipsilateral

interneurons disrupts left-right locomotor coordination in mammalian spinal cord. In Neuron, pp. 70-83.
D' Bloice, M., Stocker C., Holzinger A. (2017). Augmentor: An Image Augmentation Library for Machine Learning. Journal of Open Source Software *2*.
Delogu, A., Sellers, K., Zagoraiou, L., Bocianowska-Zbrog, A., Mandal, S., Guimera, J., Rubenstein, J.L.R., Sugden, D., Jessell, T., and Lumsden, A. (2012). Subcortical Visual Shell Nuclei Targeted by ipRGCs Develop from a Sox14+-GABAergic Progenitor and Require Sox14 to Regulate Daily Activity Rhythms. In Neuron, pp. 648-662.
Evangelio, M., García-Amado, M., and Clascá, F. (2018). Thalamocortical Projection Neuron and Interneuron Numbers in the Visual Thalamic Nuclei of the Adult C57BL/6 Mouse In Frontiers in Neuroanatomy pp. 27.
Gelman, D., Griveau, A., Dehorter, N., Teissier, A., Varela, C., Pla, R., Pierani, A., and Marin, O. (2011). A wide diversity of cortical GABAergic interneurons derives from the embryonic preoptic area. J Neurosci *31*, 16570-16580.
Golden, J.A., and Cepko, C.L. (1996). Clones in the chick diencephalon contain multiple cell types and siblings are widely dispersed. In Development, pp. 65-78.
Golding, B., Pouchelon, G., Bellone, C., Murthy, S., Di Nardo, A.A., Govindan, S., Ogawa, M., Shimogori, T., Lüscher, C., Dayer, A.*, et al.* (2014). Retinal Input Directs the Recruitment of Inhibitory Interneurons into Thalamic Visual Circuits. In Neuron, pp. 1057-1069.
Granda, R.H., and Crossland, W.J. (1989). GABA-like immunoreactivity of neurons in the chicken diencephalon and mesencephalon. In Journal of Comparative Neurology (John Wiley & Sons, Ltd), pp. 455-469.
Groh, A., Bokor, H., Mease, R.A., Plattner, V.M., Hangya, B., Stroh, A., Deschenes, M., and Acsády, L. (2014). Convergence of cortical and sensory driver inputs on single thalamocortical cells. In Cerebral Cortex (Oxford University Press), pp. 3167-3179.
Guillery, R.W. (1995). Anatomical evidence concerning the role of the thalamus in corticocortical communication: a brief review. In Journal of anatomy, pp. 583-592.
Guo, Q., and Li, J.Y.H. (2019). Defining developmental diversification of diencephalon neurons through single-cell gene expression profiling. In Development, pp. dev.174284.
Guo, Z.V., Inagaki, H.K., Daie, K., Druckmann, S., Gerfen, C.R., and Svoboda, K. (2017). Maintenance of persistent activity in a frontal thalamocortical loop. In Nature (Macmillan Publishers Limited, part of Springer Nature. All rights reserved.), pp. 181.
Halassa, M.M., and Kastner, S. (2017). Thalamic functions in distributed cognitive control. In Nature Neuroscience, pp. 1669-1679.
Halley, A.C., and Krubitzer, L. (2019). Not all cortical expansions are the same: the coevolution of the neocortex and the dorsal thalamus in mammals. In Current Opinion in Neurobiology, pp. 78-86.
Hama, H., Hioki, H., Namiki, K., Hoshida, T., Kurokawa, H., Ishidate, F., Kaneko, T., Akagi, T., Saito, T., Saido, T.*, et al.* (2015). ScaleS: an optical clearing palette for biological imaging. In Nature Neuroscience (Nature Publishing Group, a division of Macmillan Publishers Limited. All Rights Reserved.), pp. 1518.
Hayes, S.G., Murray, K.D., and Jones, E.G. (2003). Two epochs in the development of gamma-aminobutyric acidergic neurons in the ferret thalamus. In The Journal of Comparative Neurology, pp. 45-65.
Herkenham, M. (1980). Laminar organization of thalamic projections to the rat neocortex. In Science, pp. 532 LP - 535.
Hippenmeyer, S., Vrieseling, E., Sigrist, M., Portmann, T., Laengle, C., Ladle, D.R., and Arber, S. (2005). A developmental switch in the response of DRG neurons to ETS transcription factor signaling. In PLoS biology (Public Library of Science), pp. e159-e159.
Hirsch, J.A., Wang, X., Sommer, F.T., and Martinez, L.M. (2015). How Inhibitory Circuits in the Thalamus Serve Vision. In Annual Review of Neuroscience, pp. 309-329.
Hubel, D.H., and Wiesel, T.N. (1962). Receptive fields, binocular interaction and functional architecture in the cat's visual cortex. In The Journal of physiology, pp. 106-154.

Huisman, C., Cho, H., Brock, O., Lim, S.J., Youn, S.M., Park, Y., Kim, S., Lee, S.K., Delogu, A., and Lee, J.W. (2019). Single cell transcriptome analysis of developing arcuate nucleus neurons uncovers their key developmental regulators. Nat Commun *10*, 3696.

Hunnicutt, B.J., Long, B.R., Kusefoglu, D., Gertz, K.J., Zhong, H., and Mao, T. (2014). A comprehensive thalamocortical projection map at the mesoscopic level. In Nature Neuroscience (Nature Research), pp. 1276-1285.

Jager, P., Ye, Z., Yu, X., Zagoraiou, L., Prekop, H.-T., Partanen, J., Jessell, T.M., Wisden, W., Brickley, S.G., and Delogu, A. (2016). Tectal-derived interneurons contribute to phasic and tonic inhibition in the visual thalamus. In Nature Communications (Nature Publishing Group), pp. 13579.

Jones, E. (2002). Dichronous appearance and unusual origins of GABA neurons during development of the mammalian thalamus. In Thalamus & Related Systems (No longer published by Elsevier), pp. 283-288.

Jones, E., Oliphant, T., Peterson, P., and others. SciPy: Open source scientific tools for Python.

Jones, E.G. (2007). The thalamus (Cambridge University Press).

Kenigfest, N.B., Repérant, J., Rio, J.-P., Belekhova, M.G., Tumanova, N.L., Ward, R., Vesselkin, N.P., Herbin, M., Chkeidze, D.D., and Ozirskaya, E.V. (1995). Fine structure of the dorsal latreral geniculate nucleus of the turtle, Emys orbicularis: A Golgi, combined hrp tracing and GABA immunocytochemical study. In Journal of Comparative Neurology (John Wiley & Sons, Ltd), pp. 595-614.

Kenigfest, N.B., Repérant, J., Rio, J.-P., Belekhova, M.G., Ward, R., Vesselkin, N.P., Miceli, D., and Herbin, M. (1998). Retinal and cortical afferents to the dorsal lateral geniculate nucleus of the turtle, Emys orbicularis: A combined axonal tracing, glutamate, and GABA immunocytochemical electron microscopic study. In Journal of Comparative Neurology (John Wiley & Sons, Ltd), pp. 470-490.

Kimmel, R.A., Turnbull, D.H., Blanquet, V., Wurst, W., Loomis, C.A., and Joyner, A.L. (2000). Two lineage boundaries coordinate vertebrate apical ectodermal ridge formation. In Genes & Development pp. 1377-1389.

Klein, S., Staring, M., Murphy, K., Viergever, M.A., and Pluim, J.P. (2010). elastix: a toolbox for intensity-based medical image registration. IEEE Trans Med Imaging *29*, 196-205.

Lavdas, A.A., Grigoriou, M., Pachnis, V., and Parnavelas, J.G. (1999). The medial ganglionic eminence gives rise to a population of early neurons in the developing cerebral cortex. J Neurosci *19*, 7881-7888.

Lein, E.S., Hawrylycz, M.J., Ao, N., Ayres, M., Bensinger, A., Bernard, A., Boe, A.F., Boguski, M.S., Brockway, K.S., Byrnes, E.J.*, et al.* (2006). Genome-wide atlas of gene expression in the adult mouse brain. In Nature (Nature Publishing Group), pp. 168.

Letinić, K., and Kostović, I. (1997). Transient fetal structure, the gangliothalamic body, connects telencephalic germinal zone with all thalamic regions in the developing human brain. In Journal of Comparative Neurology (John Wiley & Sons, Ltd), pp. 373-395.

Letinic, K., and Rakic, P. (2001). Telencephalic origin of human thalamic GABAergic neurons. In Nature Neuroscience, pp. 931-936.

Ling, S., Pratte, M.S., and Tong, F. (2015). Attention alters orientation processing in the human lateral geniculate nucleus. In Nature neuroscience, pp. 496-498.

Marín, O., and Rubenstein, J.L.R. (2001). A long, remarkable journey: Tangential migration in the telencephalon. In Nature Reviews Neuroscience, pp. 780-790.

Martinez, S., and Alvarado-Mallart, R.M. (1989). Transplanted mesencephalic quail cells colonize selectively all primary visual nuclei of chick diencephalon: a study using heterotopic transplants. In Brain research Developmental brain research, pp. 263-274.

McKinney, W. (2010). Data Structures for Statistical Computing in Python. In Proceedings of the 9th Python in Science Conference, S. van der Walt, and J. Millman, eds., pp. 51-56.

Métin, C., Alvarez, C., Moudoux, D., Vitalis, T., Pieau, C., and Molnár, Z. (2007). Conserved pattern of tangential neuronal migration during forebrain development. In Development, pp. 2815 LP - 2827.

Miller, J.A., Ding, S.-L., Sunkin, S.M., Smith, K.A., Ng, L., Szafer, A., Ebbert, A., Riley, Z.L., Royall, J.J., Aiona, K.*, et al.* (2014). Transcriptional landscape of the prenatal human brain. In Nature (Nature Publishing Group, a division of Macmillan Publishers Limited. All Rights Reserved.), pp. 199.

Mo, A., Mukamel, E.A., Davis, F.P., Luo, C., Henry, G.L., Picard, S., Urich, M.A., Nery, J.R., Sejnowski, T.J., Lister, R.*, et al.* (2015). Epigenomic Signatures of Neuronal Diversity in the Mammalian Brain. In Neuron, pp. 1369-1384.

Monory, K., Massa, F., Egertová, M., Eder, M., Blaudzun, H., Westenbroek, R., Kelsch, W., Jacob, W., Marsch, R., Ekker, M.*, et al.* (2006). The endocannabinoid system controls key epileptogenic circuits in the hippocampus. In Neuron, pp. 455-466.

Montero, V.M. (1987). Ultrastructural identification of synaptic terminals from the axon of type 3 interneurons in the cat lateral geniculate nucleus. In Journal of Comparative Neurology (John Wiley & Sons, Ltd), pp. 268-283.

Motulsky, H.J., and Brown, R.E. (2006). Detecting outliers when fitting data with nonlinear regression - a new method based on robust nonlinear regression and the false discovery rate. BMC Bioinformatics *7*, 123.

Paredes, M.F., James, D., Gil-Perotin, S., Kim, H., Cotter, J.A., Ng, C., Sandoval, K., Rowitch, D.H., Xu, D., McQuillen, P.S.*, et al.* (2016). Extensive migration of young neurons into the infant human frontal lobe. In Science, pp. aaf7073.

Pasik, P., Pasik, T., and Hámori, J. (1976). Synapses between interneurons in the lateral geniculate nucleus of monkeys. In Experimental brain research, pp. 1-13.

Penny, G.R., Conley, M., Schmechel, D.E., and Diamond, I.T. (1984). The distribution of glutamic acid decarboxylase immunoreactivity in the diencephalon of the opossum and rabbit. J Comp Neurol *228*, 38-56.

Piscopo, D.M., El-Danaf, R.N., Huberman, A.D., and Niell, C.M. (2013). Diverse Visual Features Encoded in Mouse Lateral Geniculate Nucleus. In The Journal of Neuroscience, pp. 4642 LP - 4656.

Prekop, H.-T., Kroiss, A., Rook, V., Zagoraiou, L., Jessell, T.M., Fernandes, C., Delogu, A., and Wingate, R.J.T. (2018). Sox14 Is Required for a Specific Subset of Cerebello–Olivary Projections. In The Journal of Neuroscience, pp. 9539 LP - 9550.

Pritz, M.B., and Stritzel, M.E. (1994). Morphological and GAD immunocytochemical properties of the dorsal lateral geniculate nucleus in a reptile. In Brain Research Bulletin, pp. 723-726.

Puelles, L., and Rubenstein, J.L.R. (2003). Forebrain gene expression domains and the evolving prosomeric model. In Trends in Neurosciences, pp. 469-476.

Ragan, T., Kadiri, L.R., Venkataraju, K.U., Bahlmann, K., Sutin, J., Taranda, J., Arganda-Carreras, I., Kim, Y., Seung, H.S., and Osten, P. (2012). Serial two-photon tomography for automated ex vivo mouse brain imaging. Nat Methods *9*, 255-258.

Rakić, P., and Sidman, R.L. (1969). Telencephalic origin of pulvinar neurons in the fetal human brain. In Zeitschrift für Anatomie und Entwicklungsgeschichte, pp. 53-82.

Rausell, E., and Jones, E.G. (1991). Histochemical and immunocytochemical compartments of the thalamic VPM nucleus in monkeys and their relationship to the representational map. J Neurosci *11*, 210-225.

Rikhye, R.V., Gilra, A., and Halassa, M.M. (2018a). Thalamic regulation of switching between cortical representations enables cognitive flexibility. In Nature Neuroscience, pp. 1753-1763.

Rikhye, R.V., Wimmer, R.D., and Halassa, M.M. (2018b). Toward an Integrative Theory of Thalamic Function. In Annual Review of Neuroscience (Annual Reviews), pp. 163-183.

Rio, J.-P., Reperant, J., Ward, R., Miceli, D., and Medina, M. (1992). Evidence of GABA-immunopositive neurons in the dorsal part of the lateral geniculate nucleus of reptiles: Morphological correlates with interneurons. In Neuroscience, pp. 395-407.

Ronneberger O., F.P., Brox T. (2015). U-Net: Convolutional Networks for Biomedical Image Segmentation (Springer, Cham).

Rousseeuw, P.J. (1987). Silhouettes: A graphical aid to the interpretation and validation of cluster analysis. In Journal of Computational and Applied Mathematics, pp. 53-65.

Rubio-Garrido, P., Pérez-de-Manzo, F., Porrero, C., Galazo, M.J., and Clascá, F. (2009). Thalamic Input to Distal Apical Dendrites in Neocortical Layer 1 Is Massive and Highly Convergent. In Cerebral Cortex, pp. 2380-2395.

Saalmann, Y.B., and Kastner, S. (2011). Cognitive and Perceptual Functions of the Visual Thalamus. In Neuron, pp. 209-223.

Saunders, A., Macosko, E.Z., Wysoker, A., Goldman, M., Krienen, F.M., de Rivera, H., Bien, E., Baum, M., Bortolin, L., Wang, S.*, et al.* (2018). Molecular Diversity and Specializations among the Cells of the Adult Mouse Brain. In Cell, pp. 1015-1030.e1016.

Schindelin, J., Rueden, C.T., Hiner, M.C., and Eliceiri, K.W. (2015). The ImageJ ecosystem: An open platform for biomedical image analysis. Mol Reprod Dev *82*, 518-529.

Schmitt, L.I., Wimmer, R.D., Nakajima, M., Happ, M., Mofakham, S., and Halassa, M.M. (2017). Thalamic amplification of cortical connectivity sustains attentional control. In Nature (Nature Research), pp. 219-223.

Seabrook, T.A., El-Danaf, R.N., Krahe, T.E., Fox, M.A., and Guido, W. (2013a). Retinal Input Regulates the Timing of Corticogeniculate Innervation. In Journal of Neuroscience, pp. 10085-10097.

Seabrook, T.A., Krahe, T.E., Govindaiah, G., and Guido, W. (2013b). Interneurons in the mouse visual thalamus maintain a high degree of retinal convergence throughout postnatal development. In Neural Development (BioMed Central), pp. 24.

Sellers, K., Zyka, V., Lumsden, A.G., and Delogu, A. (2014). Transcriptional control of GABAergic neuronal subtype identity in the thalamus. Neural Dev *9*, 14.

Sgaier, S.K., Lao, Z., Villanueva, M.P., Berenshteyn, F., Stephen, D., Turnbull, R.K., and Joyner, A.L. (2007). Genetic subdivision of the tectum and cerebellum into functionally related regions based on differential sensitivity to engrailed proteins. In Development (NIH Public Access), pp. 2325-2335.

Shatz, C.J. (1996). Emergence of order in visual system development. In Proceedings of the National Academy of Sciences, pp. 602 LP - 608.

Sherman, S.M. (2004). Interneurons and triadic circuitry of the thalamus. In Trends in Neurosciences, pp. 670-675.

Sherman, S.M. (2016). Thalamus plays a central role in ongoing cortical functioning. In Nature Neuroscience (Nature Research), pp. 533-541.

Sherman, S.M., and Guillery, R.W. (2002). The role of the thalamus in the flow of information to the cortex. In Philosophical Transactions of the Royal Society of London Series B: Biological Sciences (Royal Society), pp. 1695-1708.

Shi, W., Xianyu, A., Han, Z., Tang, X., Li, Z., Zhong, H., Mao, T., Huang, K., and Shi, S.-H. (2017). Ontogenetic establishment of order-specific nuclear organization in the mammalian thalamus. In Nature Neuroscience, pp. 516-528.

Sousa, V.H., Miyoshi, G., Hjerling-Leffler, J., Karayannis, T., and Fishell, G. (2009). Characterization of Nkx6-2-Derived Neocortical Interneuron Lineages. In Cerebral Cortex, pp. i1-i10.

Stephan, H., Frahm, H., and Baron, G. (1981). New and Revised Data on Volumes of Brain Structures in Insectivores and Primates. In Folia Primatologica, pp. 1-29.

Sugahara, F., Murakami, Y., Pascual-Anaya, J., and Kuratani, S. (2017). Reconstructing the ancestral vertebrate brain. In Development, Growth & Differentiation (John Wiley & Sons, Ltd (10.1111)), pp. 163-174.

Sugahara, F., Pascual-Anaya, J., Oisi, Y., Kuraku, S., Aota, S.-i., Adachi, N., Takagi, W., Hirai, T., Sato, N., Murakami, Y.*, et al.* (2016). Evidence from cyclostomes for complex regionalization of the ancestral vertebrate brain. In Nature (Nature Publishing Group, a division of Macmillan Publishers Limited. All Rights Reserved.), pp. 97.

Tasic, B., Menon, V., Nguyen, T.N., Kim, T.K., Jarsky, T., Yao, Z., Levi, B., Gray, L.T., Sorensen, S.A., Dolbeare, T.*, et al.* (2016). Adult mouse cortical cell taxonomy revealed by single cell transcriptomics. In Nature Neuroscience (Nature Research), pp. 335-346.

Tasic, B., Yao, Z., Graybuck, L.T., Smith, K.A., Nguyen, T.N., Bertagnolli, D., Goldy, J., Garren, E., Economo, M.N., Viswanathan, S.*, et al.* (2018). Shared and distinct transcriptomic cell types across neocortical areas. In Nature, pp. 72-78.

Thompson, A.D., Picard, N., Min, L., Fagiolini, M., and Chen, C. (2016). Cortical Feedback Regulates Feedforward Retinogeniculate Refinement. In Neuron (Elsevier), pp. 1021-1033.

Tosches, M.A., Yamawaki, T.M., Naumann, R.K., Jacobi, A.A., Tushev, G., and Laurent, G. (2018). Evolution of pallium, hippocampus, and cortical cell types revealed by single-cell transcriptomics in reptiles. In Science, pp. 881 LP - 888.

Tremblay, R., Lee, S., and Rudy, B. (2016). GABAergic Interneurons in the Neocortex: From Cellular Properties to Circuits. In Neuron, pp. 260-292.

Van der Loos, H., and Woolsey, T.A. (1973). Somatosensory Cortex: Structural Alterations following Early Injury to Sense Organs. In Science, pp. 395 LP - 398.

Veenman, C.L., and Reiner, A. (1994). The distribution of GABA-containing perikarya, fibers, and terminals in the forebrain and midbrain of pigeons, with particular reference to the basal ganglia and its projection targets. In Journal of Comparative Neurology (John Wiley & Sons, Ltd), pp. 209-250.

Walt, S.v.d., Colbert, S.C., and Varoquaux, G. (2011). The NumPy Array: A Structure for Efficient Numerical Computation. In Computing in Science & Engineering (IEEE Computer Society), pp. 22-30.

Watakabe, A., Ohsawa, S., Hashikawa, T., and Yamamori, T. (2006). Binding and complementary expression patterns of semaphorin 3E and plexin D1 in the mature neocortices of mice and monkeys. J Comp Neurol *499*, 258-273.

Wichterle, H., Turnbull, D.H., Nery, S., Fishell, G., and Alvarez-Buylla, A. (2001). In utero fate mapping reveals distinct migratory pathways and fates of neurons born in the mammalian basal forebrain. Development *128*, 3759-3771.

Wong, S.Z.H., Scott, E.P., Mu, W., Guo, X., Borgenheimer, E., Freeman, M., Ming, G.-l., Wu, Q.-F., Song, H., and Nakagawa, Y. (2018). In vivo clonal analysis reveals spatiotemporal regulation of thalamic nucleogenesis. In PLOS Biology (Public Library of Science), pp. e2005211.

Xu, Q., Cobos, I., De La Cruz, E., Rubenstein, J.L., and Anderson, S.A. (2004). Origins of cortical interneuron subtypes. J Neurosci *24*, 2612-2622.

Xu, Q., Tam, M., and Anderson, S.A. (2008). Fate mapping Nkx2.1-lineage cells in the mouse telencephalon. J Comp Neurol *506*, 16-29.

Zeater, N., Cheong, S.K., Solomon, S.G., Dreher, B., and Martin, P.R. (2015). Binocular Visual Responses in the Primate Lateral Geniculate Nucleus. In Current Biology (Elsevier), pp. 3190-3195.